universität wien

DISSERTATION / DOCTORAL THESIS

Titel der Dissertation / Title of the Doctoral Thesis

Strategies for generating, distributing and certifying entanglement in photonic systems

verfasst von / submitted by

Dipl. Ing. Lukas Achatz, BSc

angestrebter akademischer Grad / in partial fulfilment of the requirements for the degree of

Doktor der Naturwissenschaften (Dr. rer. nat.)

Wien, 2023 / Vienna, 2023

Studienkennzahl lt. Studienblatt / degree programme code as it appears on the student record sheet:	UA 796 605 411
Dissertationsgebiet lt. Studienblatt / field of study as it appears on the student record sheet:	Physik
Betreut von / Supervisor:	Mag. Dr. Marcus Huber, Privatdoz.

ACKNOWLEDGMENTS

The duration of my PhD was riddled not only with typical PhD-problems, but also with lock-downs, lab-access restrictions and the fact that the group dissolved. Thus, a big thank you goes out to Marcus Huber, who took over my supervision in the very last year of my studies. I am aware of the added workload and deeply thankful for the frictionless transition.

I also want to thank Rupert Ursin for giving me the opportunity to work with some of the smartest and, at the same time, silliest people I have ever met. Despite the fact that he founded his own company he always had an open ear for my many questions and, above all, even hired me for his new company - that's on you! Without him my academic life would have taken an entirely different course, and I am very grateful it didn't.

I consider myself very lucky to say that my colleagues have now become close friends. In no particular order: Evelyn Ortega, Lukas Bulla, Martin Bohmann, Sebastian Neumann and Sebastian Ecker. All of you have made the PhD time - which often times was very isolated due to Covid - more interesting, enjoyable and endurable. Thank you Evelyn for explaining me all there is to know about aligning our source and the multi-core fiber. More than once was I convinced to have destroyed everything, just for you to fix it within minutes. I want to thank Lukas for always helping me with any technical difficulties I had to overcome, be it the stabilization of a laser, an interferometer or my nerves after something broke for the hundredth time. Martin - the theoretician we neither needed nor deserved - thank you for your constant guidance in regards to writing my publications and the not-so-constant supply of Bavarian beer. Sebastian Neumann, thank you for teaching me the principles of fibers, detectors and backgammon - I'm sure at some point you can beat my (in every way superior) strategy. Sebastian Ecker, thank you for your valuable insights into, well, everything science related. I enjoy every time we go climbing together - what you lack in climbing skills you make up for in belaying.

I also want to thank my parents, without whom my education would have been

hardly possible. I am very grateful that I can always count on you no matter what, I know this is not a given and how blessed I am to have you. Thanks to my girlfriend Carina for always being there for me, listening to my complaints and guiding me back on track.

ABSTRACT

Quantum entanglement is at the heart of many applications in the field of quantum information processing. In many cases a vital part is to faithfully generate, distribute and verify the existing entanglement. Since its first theoretical description, a multitude of different techniques have been developed for achieving these goals. When transitioning from a protected laboratory environment to real-world scenarios, decoherence and inevitable loss of photons fundamentally limits the extractable information. It is thus desirable to encode as much information per photon as possible. In this sense, an important feature of entanglement-based photonic systems is the fact that photons can be simultaneously entangled in multiple degrees of freedom, referred to as hyper-entanglement. When working with hyper-entangled states, a crucial part is understanding the various tunable parameters of the entanglement source as well as which technique to apply for its certification and quantification. In this cumulative thesis I will present three publications guiding through the process of generating, distributing and eventually certifying entanglement in various degrees of freedom. In the first publication the process for generating entanglement is extensively studied and compared to theoretical predictions. The second publication is concerned with the distribution of a hyper-entangled state in polarization, energy-time and path as well as its subsequent verification. In the third publication another method for certifying position-momentum entanglement is applied which helps in understanding the entire wave function created by our entanglement source. In summary, this thesis is concerned with the creation, distribution and certification of photonic entanglement in various degrees of freedom.

KURZFASSUNG

Die Quantenverschränkung steht im Mittelpunkt vieler Anwendungen auf dem Gebiet der Quanteninformationsverarbeitung. In vielen Fällen besteht ein wesentlicher Teil darin, die vorhandene Verschränkung adäquat zu erzeugen, zu verteilen und zu verifizieren. Um dieses Ziel zu erreichen wurden bereits eine VIelzahl verschiedener Technicken entwickelt. Beim Übergang von einer geschützten Laborumgebung zu realen Szenarien wird die extrahierbare Information von Dekohärenz sowie dem unvermeidlichen Verlust von Photonen grundlegend limitiert. Ziel ist es daher, ein Maximum an Information pro versendetem Photon zu kodieren. In diesem Sinne ist die Hyperverschränkung, also die Verschränkung von Photonen in mehreren Freiheitsgraden gleichzeitig, ein wichtiger Bestandteil. Bei der Arbeit mit hyperverschränkten Zuständen ist es von entscheidender Bedeutung, die unterschiedlichen verstellbaren Parameter der Verschränkungsquelle zu verstehen und zu wissen, welche Technik für deren Nachweis und Quantifizierung anzuwenden ist. In dieser kumulativen Dissertation stelle ich drei Publikationen vor, welche durch den Prozess der Erzeugung, Verteilung und schließlich Zertifizierung von Verschränkung in verschiedenen Freiheitsgraden führen. In der ersten Publikation wird der Prozess zur Erzeugung der Verschränkung eingehend untersucht und mit theoretischen Vorhersagen verglichen. Die zweite Publikation befasst sich mit der Verteilung eines hyperverschränkten Zustands in Polarisation, Energie-Zeit und Pfad sowie seiner anschließenden Verifizierung. In der dritten Publikation wird eine weitere Methode zum Nachweis der Verschränkung in Position-Impuls angewandt, welche zum Verständnis der gesamt erzeugten Wellenfunktion beiträgt. Zusammengefasst beschäftigt sich diese Arbeit mit der Erzeugung, Verteilung und Zertifizierung von photonischer Verschränkung in verschiedenen Freiheitsgraden.

LIST OF PUBLICATIONS

Peer-reviewed

- **Spatial and spectral characterization of photon pairs at telecommunication-wavelength from type-0 spontaneous parametric down-conversion**
  Evelyn A. Ortega, Jorge Fuenzalida, Mirela Selimovic, Krishna Dovzhik, Lukas Achatz, Sören Wengerowsky, Rodrigo F. Shiozaki, Sebastian P. Neumann, Martin Bohmann and Rupert Ursin
  ⟶ **Section 3.1**
  Journal of the Optical Society of America B Vol. 40, Issue 1, pp. 165-171 (2023)

- **Simultaneous transmission of hyper-entanglement in 3 degrees of freedom through a multicore fiber**
  Lukas Achatz, Lukas Bulla, Sebastian Ecker, Evelyn A. Ortega, Michael Bartokos, Martin Bohmann, Rupert Ursin and Marcus Huber
  ⟶ **Section 3.2**
  npj Quantum Information volume 9, Article number: 45 (2023)

- **Certifying position-momentum entanglement at telecommunication wavelengths**
  Lukas Achatz, Evelyn A Ortega, Krishna Dovzhik, Rodrigo F Shiozaki, Jorge Fuenzalida, Sören Wengerowsky, Martin Bohmann and Rupert Ursin
  ⟶ **Section 3.3**
  Physica Scripta 97, 015101 (2021)

- **Experimental wavelength-multiplexed entanglement-based quantum cryptography**
  Johannes Pseiner, Lukas Achatz, Lukas Bulla, Martin Bohmann and Rupert Ursin
  Quantum Science and Technology 6, 035013 (2021)

CONTENTS

CHAPTER 1

INTRODUCTION

The aim of this introduction is to give a brief overview of the theoretical concept which was studied during this thesis, namely *quantum entanglement*. Entanglement is a fundamental property of quantum mechanics and has been experimentally verified for a variety of different fundamental particles such as photons [1], neutrinos [2] and electrons [3], just to name a few. Transmitting information through the use of entangled photons features advantages not met by its classical counterparts, among others, based on the fundamental unclonability of quantum states [4]. The publications in this work concentrate solely on entanglement-based photonic systems, which can be used in a multitude of different technical applications, ranging from quantum key distribution [5, 6, 7] to superdense coding [8, 9, 10], quantum computation [11, 12, 13] and teleportation [14, 15]. In the last decades the field of quantum information has seen rapid progress, with a remarkable increase of scientific publications proposing various ways to study entanglement. For this reason I will limit the following discussions exclusively on the techniques applied within this thesis.

In section 1.1 I will briefly explain the history of quantum entanglement since its first conception. In chapter 2 I will lead through the processes used in this thesis for generating, distributing and finally certifying entanglement. Lastly, in chapter 3, the scientific publications are printed in original.

1.1 Quantum entanglement

The first description of quantum entanglement dates back to a famous publication by Einstein, Podolsky and Rosen in 1935 [16], where they introduced what is now known as local realism. The argumentation is based on following two premises:

Realism: If, without in any way disturbing a system, we can predict with certainty (i.e., with probability equal to unity) the value of a physical quantity, then there exists an element of physical reality corresponding to this physical quantity.

Locality: A measurement performed at a spatially separated location x_1 cannot change the outcome of a measurement performed at a location x_2.

In the gedankenexperiment EPR considered two particles, A and B, which are created at the same time $t = 0$ travelling to two users, Alice and Bob, with opposite momentum vectors $\mathbf{p}_A = -\mathbf{p}_B$. Since Alice is free to choose whether she measures the momentum or the position of her particle, there has to simultaneously exist an element of physical reality corresponding to those physical quantities. A measurement of particle A at Alice's site instantaneously defines the state of particle B at Bob's site. Furthermore, since the Heisenberg uncertainty principle [17] does not allow arbitrarily precise measurements on two non-commuting observables, EPR argued that quantum mechanics cannot be considered complete and there exist "hidden variables" not described by the wave function. Those hidden variables would be intrinsic to each particle, such that a measurement at Alice's site would not instantaneously define the state of Bob's particle, since the information about the measurement outcome has been hidden in Bob's particle all along, but rather just reveal one possibility of it, thus getting rid of what Einstein called "spooky action at a distance". It is worth mentioning that this does not enable superluminal communication, since the measurement outcome is still completely random [18]. As will be explained in section 2.3 several different approaches have been developed to disprove EPR's argument.

When talking about quantum entanglement from a mathematical standpoint, the possible states of a quantum system are defined as state vectors in an abstract Hilbert space. A quantum state of two particles can be considered entangled if its wave function cannot be written as a tensor product of the individual wave functions, i. e. $|\psi\rangle_{AB} \neq |\psi\rangle_A \otimes |\psi\rangle_B$. For a two-dimensional quantum entangled system a natural basis are the

so-called Bell-states, defined as:

$$\begin{aligned}
\left|\phi^{+}\right\rangle &= \frac{1}{\sqrt{2}}\left(|0\rangle_A|0\rangle_B + |1\rangle_A|1\rangle_B\right) \\
\left|\phi^{-}\right\rangle &= \frac{1}{\sqrt{2}}\left(|0\rangle_A|0\rangle_B - |1\rangle_A|1\rangle_B\right) \\
\left|\psi^{+}\right\rangle &= \frac{1}{\sqrt{2}}\left(|0\rangle_A|1\rangle_B + |1\rangle_A|0\rangle_B\right) \\
\left|\psi^{-}\right\rangle &= \frac{1}{\sqrt{2}}\left(|0\rangle_A|1\rangle_B - |1\rangle_A|0\rangle_B\right)
\end{aligned} \tag{1.1}$$

where $|0\rangle$ and $|1\rangle$ denote the orthogonal state vectors $\begin{pmatrix}1\\0\end{pmatrix}$ and $\begin{pmatrix}0\\1\end{pmatrix}$ and the indices A and B refer to the different measurement sites at Alice and Bob. If, for example, a $|\phi^{+}\rangle$ state is created and Alice measures photon A to be in the state $|0\rangle$, then she knows with certainty that Bob's photon B will also be in the state $|0\rangle$. For an in-depth explanation on the so-called Dirac-notation the reader is referred to [19].

When transitioning from the theoretical description of the wave-function to a real-world scenario, as is the case in experiments, one can ask the question of what the state-vectors actually represent. In the end, the state-vector always represents a click at a detector. However, the experimental setup for analyzing the state has to be understood in its entirety in order for the experimenter to come to a satisfying conclusion. This is especially the case if the photons are entangled simultaneously in multiple degrees of freedom (DOF), called hyper-entanglement, since a different experimental setup and consequently theoretical model is needed for each DOF. The photons' wave-function can be entangled in a variety of different DOFs, such as energy-time [20], polarization [1], position-momentum [21], orbital angular momentum [22], frequency [23] and photon number [24]. In the following chapter the DOFs used in this thesis, namely polarization, energy-time and path will be explained in more detail.

CHAPTER 2
EXPERIMENTAL IMPLEMENTATION

The publications in this thesis are concerned with entanglement in position-momentum as well as simultaneous entanglement in the properties of polarization, energy-time and path, called hyper-entanglement [25]. There exists a magnitude of various methods for creating, distributing and eventually detecting entanglement, which can vary when working with multiple DOFs [26, 27, 28, 29].

In order to faithfully generate, transmit and certify each DOF, careful considerations about the experimental setup and which theoretical model to use have to precede the implementations, which will be explained in the following sections.

2.1 Generating entanglement

The process for generating the entangled photon pairs used in this work is called type-0 spontaneous parametric down-conversion (SPDC), where one pump-photon is annihilated, subsequently creating two photons [30]. Because of energy $\omega_p = \omega_s + \omega_i$ and momentum conservation $\mathbf{p}_p = \mathbf{p}_s + \mathbf{p}_i$, the down-converted photons are entangled in energy-time and position-momentum. Here, ω_i stands for the frequency of the photons and $\mathbf{p}_i$ is the momentum vector. The indices stand for pump, signal and idler photon respectively. For a thorough description on SPDC the reader is referred to Chapter 2 in **publication** 3.1. When arranging the non-linear crystal in a Sagnac-configuration [31], additionally polarization entanglement can be produced. This leads to a hyper-entangled

wave function which is a tensor product of the wave functions of each DOF:

$$|\Psi\rangle_{\text{Total}} = |\psi\rangle_{\text{Time}} \otimes |\psi\rangle_{\text{Polarization}} \otimes |\psi\rangle_{\text{Path}} \,. \tag{2.1}$$

Note that the indices for Alice and Bob are suppressed in the following description of the wave functions. The individual wave functions can be written as follows:

$$|\psi\rangle_{\text{Time}} = \frac{1}{\sqrt{2}}(|S\rangle\,|S\rangle + e^{i\phi}\,|L\rangle\,|L\rangle), \tag{2.2}$$

where $|S\rangle$ stands for the short and $|L\rangle$ for the long arm of a Franson interferometer [32].

$$|\psi\rangle_{\text{Polarization}} = \frac{1}{\sqrt{2}}(|H\rangle\,|H\rangle + e^{i\rho}\,|V\rangle\,|V\rangle), \tag{2.3}$$

where $|H\rangle$ stands for horizontal and $|V\rangle$ for vertical polarization.

$$|\psi\rangle_{\text{Path}} = \frac{1}{\sqrt{2}}(|i\rangle\,|i'\rangle - e^{i\theta}\,|j'\rangle\,|j'\rangle), \tag{2.4}$$

where $|i\rangle$ and $|i'\rangle$ stand for one opposing core pair while $|j\rangle$ and $|j'\rangle$ represents neighboring opposing cores of a multi-core fiber. Each term will be explained in more detail in section 2.3.2.

2.1.1 Intensity distribution of SPDC photons

As explained in detail in **publication** 3.1 there exist crucial dependencies between pump-wavelength, SPDC crystal temperature and poling period of the crystal in regards to the opening angle of the SPDC emission cone. For a thorough explanation on the theory of SPDC, the reader is referred to Chapter 2 in **publication** 3.1. Since the diameter of the SPDC emission cone of the entangled photons has to match the front facet of the multi-core fiber, preliminary scans in the x and y directions in the far-field plane of the SPDC cone were conducted. These x-y-scans were done for a temperature range of 74°C to 83°C with a pump wavelength of 780.026 nm, as compared to the pump wavelength of 775 nm from **publication** 3.1. The laser in these measurements was stabilized on the hyperfine transition $5^2S_{\frac{1}{2}}$ to $5^2P_{\frac{3}{2}}$ of ^{85}Rb I via Doppler-free saturation spectroscopy [33]. For the x-y-scan a single-mode fiber (SMF) was mounted in the

crystal's far-field plane on a translation stage, which in total scanned 11x11 points with a stepsize of 10 µm. The integration time at each step was 5 s. The results of which are shown in Fig. 2.1. As can be seen, for lower temperatures the SPDC cone has a ring-like shape, referred to as non-collinear, while for increasing temperatures the cone converges to the collinear case. For the temperatures 74°C to 76°C an asymmetry in the ring-structure is visible, which most likely stems from non-ideal focusing parameters. However, for all experiments within this thesis the temperature was always greater or equal to 77.5°C, where this asymmetry is no longer apparent.

In **publication** 3.1 the theory of type-0 SPDC is extensively discussed and compared to the experimental data obtained for this hyper-entanglement source. Furthermore, the emission cone of the entangled photons is measured and compared to simulations. This helps in understanding the spatial distribution of the photons as well as their correlation widths with respect to each other. Since the opening angle of the photons' emission cone strongly depends on the crystal temperature, the work conducted in **publication** 3.1 was crucial in finding an optimal temperature in order to efficiently couple the hyper-entangled photons into a multi-core fiber, which is used in **publication** 3.2. The hyper-entangled state from Eq. 2.1 is furthermore experimentally analyzed in **publication** 3.2. The multi-core fiber used for transmission will be explained in the following section.

2.2 Distributing entanglement

The most prominent ways of distributing photons is either via (horizontal) free-space links [5, 34, 35], satellites [36, 37] or through fibers [38, 39, 40, 41]. Of course, all of the above mentioned techniques have their own advantages and challenges. Owing to the fact that during the course of this thesis only fibers were used for transmission, the following discussion will be limited merely to this case, specifically to multi-core fibers. A multi-core fiber (MCF) consists of an array of many single-mode fibers inside a single cladding, as can be seen in Fig. 2.2. This represents a convenient way of transmitting many signals as one. Initially designed for classical optical communication, by transmitting multiple cores to different users one can use a technique called multiplexing, in which many signals are joined into one for compressed transmission and subsequently demultiplexed at the receiver site. With this technique the transmitted signal, and with it the information capacity, can be greatly increased, as is also desired in certain quan-

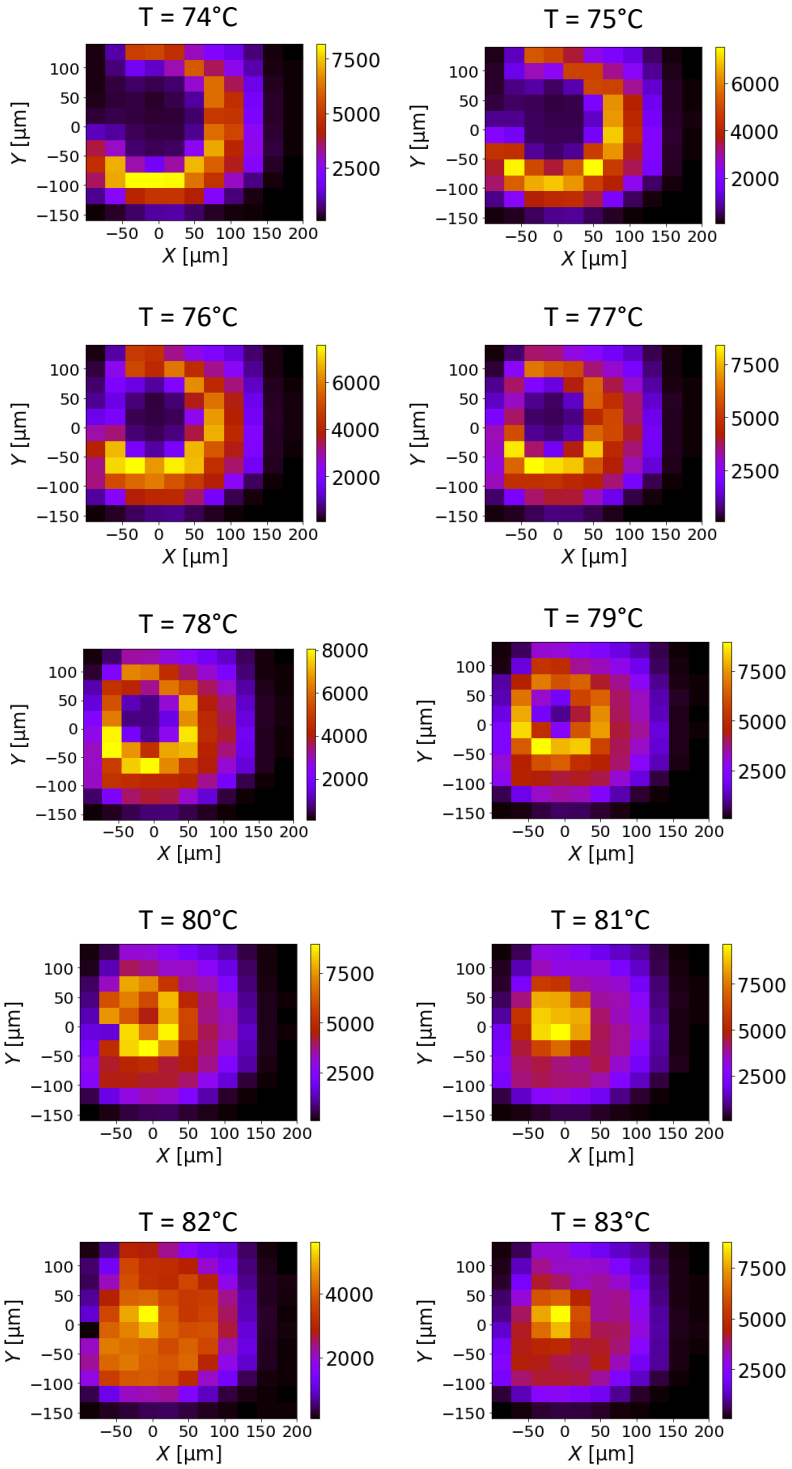

Figure 2.1: Measurement of the spatial distribution of the photon's single count rate in the far-field for crystal temperatures 74°C to 83°C.

tum information applications. An extensive review of past and existing multi-core fiber technology can be found in Ref. [42, 43]. By utilizing hyper-entangled states one can furthermore increase the channel capacity in quantum communication protocols [9, 44], effectively increasing the obtainable secure key-rate. Hyper-entanglement also proves advantageous for improved noise resilience [45, 46, 47]

In the special case of the entanglement source used in the publications presented here, an important aspect is the distinction between near- and far-field. While in the near field the position of the photons is imaged on the detection module, the momentum is imaged in the far field. Due to the aforementioned momentum-conservation it follows that $\mathbf{p}_s = -\mathbf{p}_i$, resulting in strong anti-correlations when imaging the far-field plane.

A lens setup devised in **publication** 3.1 and **publication** 3.3 allows to find optimal focusing parameters for efficiently imaging the near- and far-field plane of the crystal onto the MCF.

In **publication** 3.2 these focusing parameters are used to optimize the coupling into the MCF. Here, space division multiplexing (SDM) has been combined with hyper-entanglement in energy-time and polarization for the first time. In the second part of the same publication we successfully demonstrate the first simultaneous transmission of hyper-entanglement in energy-time, polarization and path through a MCF. This MCF consists of 19 single-mode fibers arranged in a hexagonal structure, with a length of 411m. Due to the momentum anti-correlation, the entangled photons are emitted to diametrically opposite cores of this MCF. By guiding one core to Alice and the opposing core to Bob the entangled partner-photons can thus be conveniently transmitted to each user. As already explained in section 2.1.1 the opening angle of the SPDC cone is strongly temperature dependent. Thus, finding an optimal crystal temperature is crucial for achieving high coincidence count rates. A coincidence event is defined as a simultaneous click at both detectors for Alice and Bob within a pre-defined coincidence time window, which in this case was 300 ns. In order to achieve this, the crystal temperature was scanned between 74°C to 84°C and the coincidence count rates were measured for opposing MCF pairs. When looking at the results of these measurements in Fig. 2.3, each of the 3 different ring diameters has a coincidence peak at a different temperature, which is in line with the results from the spatial distribution scans in Fig. 2.1. For lower temperatures the ring has a greater radius, resulting in coincidence peaks in the outer core pairs (01/18, 05/08, 03/11), while for increasing temperature the coincidences in

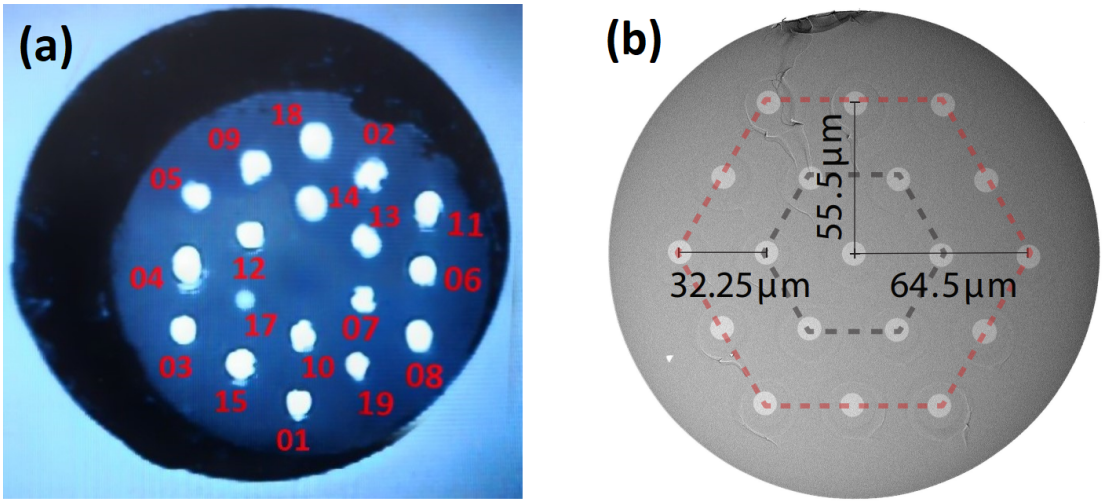

Figure 2.2: **(a)** Front facet of the MCF. Note that the center core is not shown here. **(b)** Various core distances for the single-mode fibers. Picture (b) taken from [48].

those cores decrease while in the inner cores they increase as expected. These measurements build the foundation for the experiments conducted in **publication** 3.2.

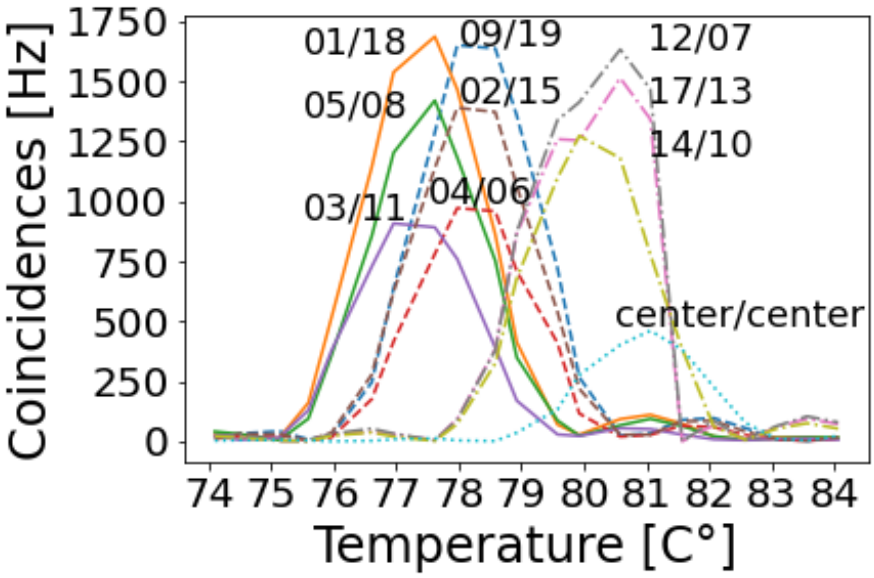

Figure 2.3: Coincidence count rates for different crystal temperatures for opposing core pairs of the MCF. The core-pair labels follow the labeling from Fig. 2.2 **(a)**. As expected, 3 distinct coincidence peaks are visible for 3 temperatures, corresponding to the 3 different ring diameters of the MCF.

2.3 Certifying entanglement

Since its first theoretical description there have been many different ways for quantitatively analyzing entanglement. The first description to experimentally test for hidden variables was proposed in [49], what is now called a Bell inequality violation, but there exist numerous ways to verify entanglement. In the following sections I will give a brief overview of the techniques used in this thesis for quantifying entanglement.

2.3.1 Schmidt number

In the literature there exist two different definitions of the Schmidt number. In the first case the Schmidt number is defined as the rank of the reduced density matrix describing the entangled state, which originates from the Schmidt decomposition [50]:

$$|\Psi\rangle = \sum_{i=0}^{N} \sqrt{\lambda_i}\,|\psi_i\rangle \otimes |\phi_i\rangle \tag{2.5}$$

where λ_i are real the eigenvalues and $|\psi_i\rangle$ and $|\phi_i\rangle$ are the eigenvectors of the decomposition. N represents the number of non-zero coefficients, i. e. the rank of the reduced density matrix $\rho_A = \mathrm{tr}_B(|\Psi\rangle\langle\Psi|)$, called Schmidt number K. This Schmidt number represents the dimensionality of a system, where for a factorizable state K = 1, for a two-dimensional polarization-entangled state K = 2 and for higher-dimensional states K > 2.

In publication [51] another measure for entanglement was introduced and also labeled Schmidt number. This approach draws from the fact that the more entangled a two-photon state, the more mixed, i. e. incoherent, its one-photon states. This method relies on the assumption that the two-photon state is pure. By measuring the overall degree of coherence [52] of one subsystem, one can use this measure to draw conclusions about the two photon state. Here, the Schmidt number is defined as the inverse purity of the reduced density matrix:

$$\tilde{\mathrm{K}} \equiv \frac{\mathrm{Tr}(\rho_B)^2}{\mathrm{Tr}(\rho_B^2)} \tag{2.6}$$

and following the calculations in [53] one arrives at following expression for the newly defined Schmidt number as a quantity for incoherence of one subsystem:

$$\tilde{\mathrm{K}} \approx \frac{1}{(2\pi)^2} \frac{[\int \mathrm{I_{NF}}(\mathbf{r}) d\mathbf{r}]^2}{\int \mathrm{I_{NF}^2}(\mathbf{r}) d\mathbf{r}} \times \frac{[\int \mathrm{I_{FF}}(\mathbf{q}) d\mathbf{q}]^2}{\int \mathrm{I_{FF}^2}(\mathbf{q}) d\mathbf{q}}, \tag{2.7}$$

where r and q stand for the position and transverse momentum vectors respectively. $\mathrm{I_{NF}}(\mathbf{r})$ is the measured intensity in the near-field and $\mathrm{I_{FF}}(\mathbf{q})$ is the measured intensity in the far-field. It is straightforward to experimentally determine these parameters and thus helps in quantifying the degree of entanglement present in the system.

In **publication** 3.1 the 'Schmidt number' (inverse purity) is measured through the intensity distribution of the photons in near- and far-field for different crystal temperatures, which is then compared to its theoretical values. The photons were probabilistically split by a beamsplitter and transmitted to a single-mode fiber mounted on a x-y translation stage (z being the propagation axis). We then scanned the x-y-plane of the photons to map the spatial distribution of the single and coincidence counts. The obtained *Schmidt numbers* are in good agreement with theory and allow to find the optimal crystal temperature for achieving a high degree of entanglement.

As a final remark it is worth mentioning that both definitions of the Schmidt number are useful quantifiers of entanglement. Both definitions are based on the eigenvalues of

the reduced density matrices. While one measures the necessary dimension needed to represent the state mathematically, the other is rather a measure for the average degree of entanglement of a quantum system. Also, the entanglement dimension Schmidt number K is mostly used in its mixed state generalization, whereas the alternative definition of the Schmidt number $\tilde{K}$ is assuming pure states.

2.3.2 Visibility fringe measurement

In **publication** 3.2 visibility fringes were measured by varying the phase between the entangled states. If one measures a visibility in a superposition basis of greater than 71%, the photons are entangled [54]. This is straightforward to see when looking at following relation:

$$S_{\max} = 2\sqrt{2}V \tag{2.8}$$

where $S_{\max}$ refers to the maximal achievable S-value and V refers to the measured visibility of the coincidence fringes, with a maximum value of 1. As Bell proved in his famous paper from 1964 [49], a violation of a Bell inequality is achieved when measuring a S value of greater than 2, i.e. $V > \frac{1}{\sqrt{2}} \approx 0.71$. Furthermore, violating a Bell inequality in turn means that non-local properties reside within the quantum system. Since entanglement is a prerequisite for non-local correlations, violating a Bell inequality is one way to certify entanglement.

As already mentioned in section 2.1, the state from **publication** 3.2 is hyper-entangled in time, path and polarization. In order to analyze entanglement in the time DOF from Eq. 2.2, two Franson interferometers [32] were used, one for Alice and one for Bob. These consist of two unbalanced Mach-Zehnder interferometers. The entangled photons have 4 possibilities of travelling through the interferometers. Either both photons take the same path, short or long, or both photons take different paths. In the first scenario one cannot temporally distinguish between the two cases. A variation of the phase difference ϕ of one interferometers leads to a sinusoidal behavior of the coincidence count rate.

Because of the detection setup as shown in Figure 1 in **publication** 3.2, the polarization DOF from Eq. 2.3 is continuously measured at each phase of the Franson interferometer.

For analyzing the path DOF of Eq. 2.4 after transmission through a MCF, two neigh-

boring cores and their opposing cores were overlapped on two separate beamsplitters, as shown in Fig. 2.4. This constitutes a superposition basis measurement in the path domain. The phase of the entangled state θ was varied by varying the distance of one core to a beamsplitter and non-local interference fringes in the coincidence count rate were observed.

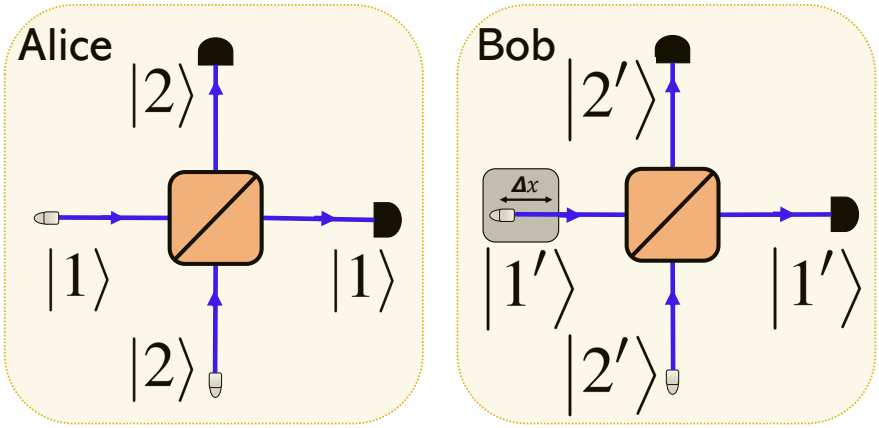

Figure 2.4: Experimental setup for measuring path visibility fringes. The entangled photon pairs enter the setup either in the spatial modes $|1\rangle$ and $|1'\rangle$ or in the modes $|2\rangle$ and $|2'\rangle$. By varying the distance to a beamsplitter of one arm the phase θ is tuned. The coincidence counts on the output ports are measured with superconducting nanowire single photon detectors (SNSPDs).

The entangled photon pairs from the source are of the form:

$$|\psi\rangle_{\text{Path}} = \frac{1}{\sqrt{2}}(|1\rangle\,|1'\rangle - e^{i\theta}\,|2\rangle\,|2'\rangle), \tag{2.9}$$

where the input modes form an orthogonal basis. The beamsplitter (BS) unitarily transforms this state via:

$$|1\rangle \overset{BS}{\Longrightarrow} \frac{1}{\sqrt{2}}\begin{pmatrix}1 & i\\ i & 1\end{pmatrix}\begin{pmatrix}1\\0\end{pmatrix} = \frac{1}{\sqrt{2}}\begin{pmatrix}1\\i\end{pmatrix} = \frac{1}{\sqrt{2}}(|1\rangle + i\,|2\rangle) \tag{2.10}$$

and for the other modes it follows analogously:

$$|1'\rangle \xrightarrow{BS} \frac{1}{\sqrt{2}}\left(|1'\rangle + i|2'\rangle\right) \tag{2.11}$$

$$|2\rangle \xrightarrow{BS} \frac{1}{\sqrt{2}}\left(i|1\rangle + |2\rangle\right) \tag{2.12}$$

$$|2'\rangle \xrightarrow{BS} \frac{1}{\sqrt{2}}\left(i|1'\rangle + |2'\rangle\right) \tag{2.13}$$

Inserting Eq. 2.10 to Eq. 2.13 into Eq. 2.9 one ends up with the final wave function after transmission through the beamsplitter:

$$|\Psi\rangle = \frac{1}{2\sqrt{2}}\left[\left(1+e^{i\theta}\right)\left(|11'\rangle - |22'\rangle\right) + \left(i - ie^{i\theta}\right)\left(|12'\rangle + |21'\rangle\right)\right] \tag{2.14}$$

By calculating the absolute square $\langle\Psi|\Psi\rangle$ one obtains the coincidence probability amplitudes P_{ij} for each output-port combination:

$$\begin{aligned} \mathrm{P}_{11'} &\propto \cos^2\left(\tfrac{\theta}{2}\right) & \mathrm{P}_{22'} &\propto \cos^2\left(\tfrac{\theta}{2}\right) \\ \mathrm{P}_{12'} &\propto \sin^2\left(\tfrac{\theta}{2}\right) & \mathrm{P}_{21'} &\propto \sin^2\left(\tfrac{\theta}{2}\right) \end{aligned} \tag{2.15}$$

In all cases the visibility was calculated with

$$V = \frac{CC_{\max} - CC_{\min}}{CC_{\max} + CC_{\min}} \tag{2.16}$$

where $CC_{max,min}$ represents the maximum and minimum value of the coincidences.

2.3.3 Inferred Heisenberg uncertainty principle

Another possibility of proofing entanglement is via a violation of Heisenberg's uncertainty principle. As already mentioned in section 1.1, EPR based their argumentation on local-realistic premises. In order to be able to experimentally verify or refute those arguments, an inferred Heisenberg uncertainty principle was introduced in [55]. By measuring correlation widths in two complementary bases to be smaller than allowed by this inequality, EPR's local-realistic premises cannot hold, thus the photons can be

considered entangled [56, 57]:

$$\Delta^2_{\text{min}}(\mathbf{r}_A|\mathbf{r}_B)\Delta^2_{\text{min}}(\mathbf{p}_A|\mathbf{p}_B) > \frac{\hbar^2}{4}, \tag{2.17}$$

$\Delta^2_{\text{min}}(\mathbf{r}_A|\mathbf{r}_B)$ is the minimum inferred variance representing the minimum uncertainty in inferring transverse position $\mathbf{r}_A$ of Alice's photon conditioned upon measuring Bob's photon $\mathbf{r}_B$ (analogously defined for the momentum $\mathbf{p}$).

In **publication** 3.3 the idea first proposed by EPR in [16] to use position-momentum entangled photons has been extensively studied. We verified position-momentum entanglement for our entanglement source by scanning the spatial distribution of the coincidence counts in the near- and far-field plane.

CHAPTER 3

PUBLICATIONS

3.1 Spatial and spectral characterization of telecommunication-wavelength photon pairs created in a type-0 MgO:ppLN crystal

In this publication the relation between SPDC emission cone, Schmidt number and temperature of the non-linear crystal is experimentally studied and compared to theory. We furthermore measured the emission spectrum of the entanglement source for different crystal temperatures. Since both the emission cone and the Schmidt number are highly temperature-dependent, finding the optimal crystal temperature is a prerequisite for the experiments to follow. The results of this publication were directly applied in **publication** 3.2.

I contributed by conducting the measurements of the photons' spatial distribution at different temperatures together with Evelyn Ortega as well as helping Mirela Selimovic in building the spectrometer and comparing the experimental data with simulations. Furthermore, I calculated the Schmidt numbers from the obtained data.

Research Article Vol. 40, No. 1 / January 2023 / Journal of the Optical Society of America B 165

Journal of the Optical Society of America B

OPTICAL PHYSICS

Spatial and spectral characterization of photon pairs at telecommunication wavelengths from type-0 spontaneous parametric downconversion

Evelyn A. Ortega,[1,2,*] Jorge Fuenzalida,[1,2,3] Mirela Selimovic,[1,2,6] Krishna Dovzhik,[1,2] Lukas Achatz,[1,2] Sören Wengerowsky,[1,2,4] Rodrigo F. Shiozaki,[5] Sebastian Philipp Neumann,[1,2] Martin Bohmann,[1] and Rupert Ursin[1,2,7]

[1]Austrian Academy of Sciences, Institute for Quantum Optics and Quantum Information-IQOQI Vienna, Boltzmanngasse 3, 1090 Vienna, Austria
[2]Vienna Center for Quantum Science and Technology (VCQ), Vienna, Austria
[3]Current address: Fraunhofer Institute for Applied Optics and Precision Engineering IOF, Albert-Einstein-Str. 7, 07745 Jena, Germany
[4]Current address: ICFO-Institut de Ciencies Fotoniques, The Barcelona Institute of Science and Technology, 08860 Castelldefels, Barcelona, Spain
[5]Departamento de Física, Universidade Federal de São Carlos, Rodovia Washington Luís, km 235—SP-310, 13565-905 São Carlos, SP, Brazil
[6]e-mail: mirela.selimovic@univie.ac.at
[7]e-mail: Rupert.Ursin@qtlabs.at
*Corresponding author: evelynacunaortega@gmail.com

Received 13 September 2022; revised 6 November 2022; accepted 28 November 2022; posted 28 November 2022; published 20 December 2022

The thorough characterization of entangled-photon sources is vital for their optimal use in quantum communication. However, this task is not trivial at telecommunication wavelengths. While cameras and spectrometers are well developed for visible and near-infrared spectra, this does not apply in the mid-infrared range. Here, we present a spatial and spectral characterization of photon pairs emitted in a type-0 phase-matched spontaneous parametric downconverted source. We experimentally show how these photon properties are modified by the crystal temperature. This parameter allows easy modification of photon-pair properties to fit multiplexing schemes based on only one entanglement photon source. Our results pave the way for the optimal design and use of spatial and spectral properties of quantum-correlated photon pairs at telecommunication wavelengths.

https://doi.org/10.1364/JOSAB.475583

1. INTRODUCTION

Nonclassical light is at the heart of a large number of applications in quantum communication [1], quantum imaging [2,3], and quantum computation [4]. For generating nonclassical light, the most well-studied and widely used process is spontaneous parametric downconversion (SPDC) [5,6]. SPDC photons can feature quantum correlations in a variety of degrees of freedom such as polarization [7], time [8,9], space [10,11], or frequency [12]. In particular, high-dimensional entangled systems have been promising in multiplexing schemes [13–15] and high-dimensional encoding [16,17].

Downconverted photons are spatially and spectrally correlated due to the momentum and energy conservation during the SPDC process. These correlations depend on the pump beam's properties and the phase-matching condition associated with the nonlinear crystal properties [18]. In periodically poled crystals, the photon-pair emission characteristics can be tuned by varying the crystal temperature [19]. In particular, it can be used to change the photon pair's spectral and spatial properties, i.e., from collinear to noncollinear propagation, as well as from degenerate to nondegenerate cases. The crystal temperature is an easily accessible parameter in entangled photon-pair source setups since it is adjusted by an electronic controller. Therefore, manipulating and optimizing spatial and spectral correlations by tuning the crystal temperature could be the way to tailor SPDC photons for desirable applications without changing optical components in the source configuration.

Spatial correlations have been thoroughly investigated for type-I and type-II phase-matched SPDC, including their dependence on the pump waist [20,21], crystal length [22], crystal temperature [23], and phase-matching condition [24]. Furthermore, the near-field correlations for type-I phase-matched SPDC have been experimentally investigated [25,26]. Type-0 phase-matched SPDC sources have exceptionally high brightness and a broad spectrum [27], which can be exploited to generate photon pairs in the telecommunication band for distribution through optical fibers [28]. These features allow for a wide range of integration into existing communication infrastructure [29,30] and the implementation of multi-user networks [31]. Recently, for photon pairs at telecommunication

wavelengths generated in type-0 phase-matched SPDC, certification of position-momentum entanglement has been done [17]. Still, spatial correlation characterization based on crystal temperature has not been implemented yet, whereas the spectral correlation has been analyzed for type-II phase-matched SPDC [32,33]. In this spectral region, there are technical difficulties in collecting and analyzing spatial and spectral distributions due to the lack of compact and efficient single-photon cameras and spectrometers.

In this paper, we study the crystal-temperature dependency of the transverse momentum and spectrum of photon pairs generated by type-0 phase-matched SPDC around 1550 nm. We implement a versatile experimental setup where the phase matching is changed through temperature control in a magnesium-oxide-doped periodically poled lithium niobate (MgO:ppLN) crystal. This analysis includes collinear and noncollinear emission scenarios. We evaluate momentum correlations of photon-pair emission through stepwise scanning at the far-field plane. Additionally, we quantify their spatial entanglement using the so-called Schmidt number. Finally, we measure the downconverted photons' spectral characteristics by a tunable wavelength filter at different crystal temperatures. Our results provide a comprehensive and precise characterization of spatial and spectral properties of photons pairs, which can help develop novel quantum communication schemes based on high-dimensional entangled systems.

The paper is structured as follows: in Section 2, we recall the theory of the type-0 phase-matched SPDC process, placing special emphasis on the temperature dependence. In Section 3, our experimental setups are explained, including the photon-pair source as well as the measurement of spatial and spectral correlations. Our results are presented and discussed in Section 4. We summarize and conclude our findings in Section 5.

2. THEORY OF TYPE-0 PHASE-MATCHING SPDC

We briefly recall the theoretical description of type-0 SPDC sources and compute the characteristics of photon pairs generated in a MgO:ppLN crystal. In SPDC, a pump photon (p) of angular frequency ω_p propagating through a nonlinear material is annihilated, creating two correlated photons labeled signal (s) and idler (i) of angular frequencies ω_s and ω_i, respectively. Let us assume that the pump photon propagates along the z axis of a periodically poled crystal with a poling period of length Λ. The SPDC process must satisfy the conservation of energy and momentum, which results in $\omega_p = \omega_s + \omega_i$, and the quasi-phase-matching (QPM) condition $\Delta\mathbf{k} = \mathbf{k}_p - \mathbf{k}_s - \mathbf{k}_i - \mathbf{k}_m$ [19], where $\mathbf{k}_p$, $\mathbf{k}_s$, and $\mathbf{k}_i$ are the wave vectors of the respective pump, signal, and idler photons, and $\mathbf{k}_m$ is the grating wave vector defined by $|\mathbf{k}_m| = 2\pi/\Lambda$. Thus, the bi-photon mode function in the momentum representation is given by [10]

$$\Phi(\mathbf{q}_s, \mathbf{q}_i, \omega_s, \omega_i) \propto E_p(\mathbf{q}_s + \mathbf{q}_i) \times \operatorname{sinc}\left(\frac{\mathrm{L}}{4\mathbf{k}_p}|\mathbf{q}_s - \mathbf{q}_i|^2 + \varphi(\mathrm{T}, \lambda)\right). \quad (1)$$

Here, L is the crystal length, and $\mathbf{q}_s$ ($\mathbf{q}_i$) is the transverse wave vector of the signal (idler) photon, i.e., $\mathbf{q}_j = (q_{x_j}, q_{y_j})$. The angular spectrum of the pump beam $E_p(\mathbf{q}_s + \mathbf{q}_i)$ typically is represented as a Gaussian function. The sinc function, called the phase-matching function, plays a crucial role in the spectral and spatial properties of the photon pairs. The collinear phase-mismatch parameter $\varphi(\mathrm{T}, \lambda)$ relates the possible wavelength combinations of the three photons (λ_p, λ_i, λ_s) and the crystal temperature T through the refractive indices n_p, n_s, and n_i, defined by the Sellmeier equation associated with the crystal [34]:

$$\varphi(T, \lambda) = \pi \mathrm{L}\left(\frac{n_p(T, \lambda_p)}{\lambda_p} - \frac{n_s(T, \lambda_s)}{\lambda_s} - \frac{n_i(T, \lambda_i)}{\lambda_i} - \frac{1}{\Lambda}\right). \quad (2)$$

The momentum conservation in the process guarantees that signal and idler photons are emitted with opposite transverse wave vectors, which means that $\mathbf{q}_s = -\mathbf{q}_i$. Hence, in the far-field plane of the crystal, we observe a photon pair distribution at opposite transverse positions, i.e., they are anti-correlated. Due to the rotational symmetry in the emission, it is sufficient to consider only one transverse coordinate to calculate the emission angle relative to the principal axis of the crystal. Thus, for the x axis,

$$\theta_j = \arctan\frac{|\mathbf{q}_{x_j}|}{|\mathbf{k}_{z_j}|}, \quad (3)$$

with $|\mathbf{k}_{z_j}|$ being the longitudinal wave vector component, where collinear emission corresponds to $\theta_j \approx 0$, i.e., signal and idler photons are emitted in the same direction as the pump photon.

To compare the theoretical predictions with our experimental results, we consider the following input parameters: pump wavelength of $\lambda_p \sim 775$ nm, crystal parameters $\mathrm{L} = 40$ mm, and $\Lambda = 19.2$ μm. We compute the spectral properties by the square modulus of the phase-matching function and the emission angle by Eq. (3), displayed in Figs. 1(a) and 1(b), respectively. Figure 1(a), for crystal temperatures from 80°C to 84°C, shows spectral degeneracy, i.e., $\lambda_i = \lambda_s$. For higher temperatures up to 88°C, photon pairs show nondegenerate wavelengths with tunability over 1490–1617 nm. Another spectral characteristic that has shown temperature dependence is the spectral bandwidth [27]. The full width at half maximum (FWHM) bandwidth is determined by crystal length and the photon pairs' group velocity mismatch, resulting in a broad spectrum close to the degenerate case. Here, the FWHM is about 60 nm and decreases in nondegenerate wavelength until ∼12 nm at $\mathrm{T} = 90$°C for signal and idler, separately. In Fig. 1(b), we observe the relation between emission angle and wavelength of photon pairs depending on the crystal temperature. Different photon-pair wavelength selections affect the emission angle at the same temperature. The blue line represents the degenerate case with $\lambda_s = \lambda_i = 1550.1$ nm, showing collinearity at $\mathrm{T} \approx 84$°C. The red line represents a nondegenerate case with $\lambda_i = 1551.72$ nm, $\lambda_s = 1548.52$ nm, which results in a collinear cone at $\mathrm{T} \approx 85$°C. In Fig. 1(c), we can see the QPM transition of signal and idler photons from noncollinear to collinear propagation from Eq. (1).

Note that Eq. (2) shows that changing the crystal temperature produces a variation on the collinear phase-mismatch parameter φ. Therefore, we must observe a substantial variation of the

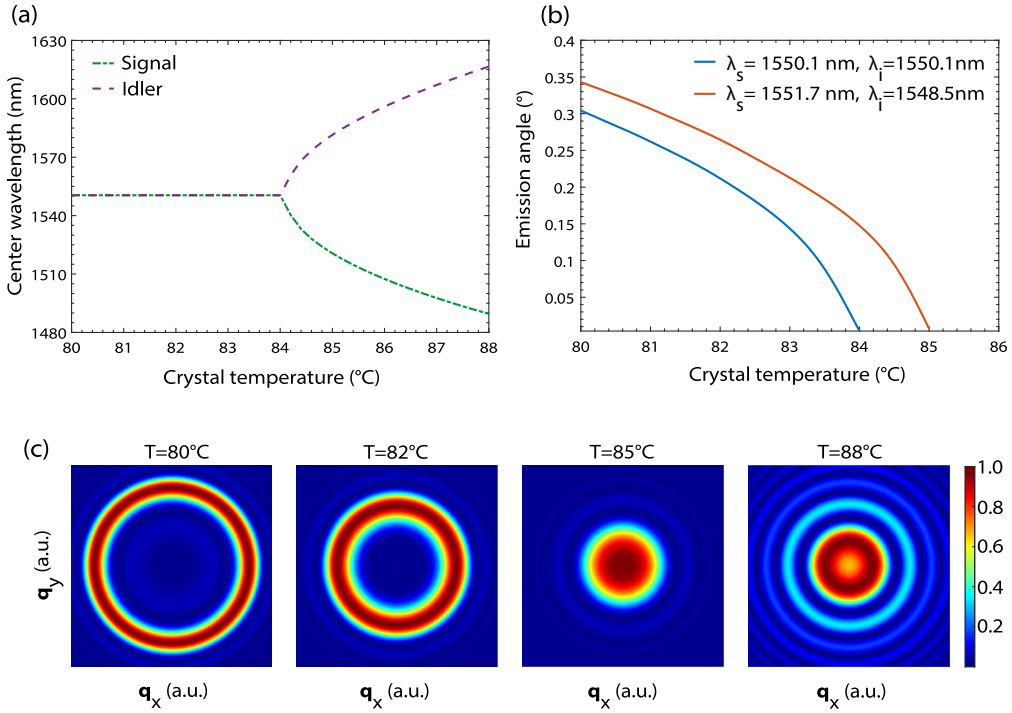

Fig. 1. (a) Numerically calculated center wavelength for photons emitted from MgO:ppLN crystal as a function of its temperature considering the emission angle is 0°. (b) Calculated emission angle of photon pairs as a function of crystal temperature. For illustration, we selected the degenerate case (blue) and a nondegenerate one (red). (c) Representation of spatial intensity distribution of the photons at the far-field plane with $\lambda_i = 1551.72$ nm and $\lambda_s = 1548.52$ nm at four crystal temperatures: 80°, 82°, 85°, and 88°C.

intensity distribution in the far field (momentum correlation) for different crystal temperature settings. In contrast, in the near field (position correlation), this remains unaffected [26] for a variation on crystal temperature. For this reason, we focus on the analysis of the momentum correlation.

3. EXPERIMENTAL IMPLEMENTATION

A. Photon-Pair Source

The experimental setup of the type-0 phase-matched SPDC source is shown in Fig. 2. A 775 nm continuous-wave (cw) pump laser is coupled into a single-mode fiber (SMF) and sent through a polarizing beam splitter (PBS) and a half-wave plate (HWP) to adjust the pump beam's polarization for which the type-0 phase matching was designed. The collimated pump beam is focused with a plano–convex lens L_0 with focal length $f_0 = 250$ mm at the center of a 40 mm long MgO:ppLN crystal with a poling period of $\Lambda = 19.2$ μm. The resulting pump waist in the center of the crystal is ∼80 μm. The nonlinear crystal is mounted in an oven allowing a homogeneous temperature distribution inside the oven where the crystal temperature is set with a precision of ±0.1°C. The emitted SPDC photons are separated from the pump beam with a dichroic mirror (DM) and spectrally cleaned with a long-pass filter (LPF). The lens L_1 is located at a focal distance $f_1 = 200$ mm from the center of the crystal, performing a Fourier transform of its transverse plane at the focal distance f_1.

B. Spatial Correlation Measurement

To analyze the spatial correlations of the photon pairs emitted by our source and its dependence on crystal temperature, we implemented scanning measurements in the near field and far field of the signal and idler mode (see Fig. 2). At the output of the source, the signal and idler photons were split probabilistically on a 50:50 beam splitter (BS). For recording the far-field plane, we implemented an imaging system $2f_2/2f_3$ ($2f_2'/2f_3'$) with lenses L_2 and L_3 (L_2' and L_3') with focal lengths of $f_2 = f_2' = 150$ mm and $f_3 = f_3' = 4.5$ mm. This configuration results in a magnification factor of $M_{FF} = 0.03$. For recording the near-field plane, the crystal's center is imaged with a $2f_1/2f_2$ ($2f_1/2f_2'$) system using lenses L_1 and L_2 (L_2') in each arm. This configuration results in a magnification factor of $M_{NF} = 0.75$.

In the near- and far-field configurations, the photon pairs were collected in their respective detection planes by two telecommunication wavelength SMFs mounted on translation stages. Due to the symmetry in SPDC photon emission, we performed for the idler a plane scan (x_i, y_i) and for the signal just a linear scan along the x axis $(x_i, y_i = 0)$. The scan was performed over 100 μm in steps of 10 μm, which were chosen following the mode field diameter of the SMF ∼10.4 μm. For each crystal temperature, we recorded $21^3 = 9261$ data points, corresponding to three-dimensional measurement settings $(x_i, y_i; x_s)$. The wavelengths of the signal and idler were filtered by appropriate wavelength-division-multiplexing (WDM) channels with a spectral FWHM of 0.6 nm. We chose wavelength channels centered at $\lambda_i = 1551.72$ nm and $\lambda_s = 1548.52$ nm for a detailed analysis, as they are close to the central wavelength. The

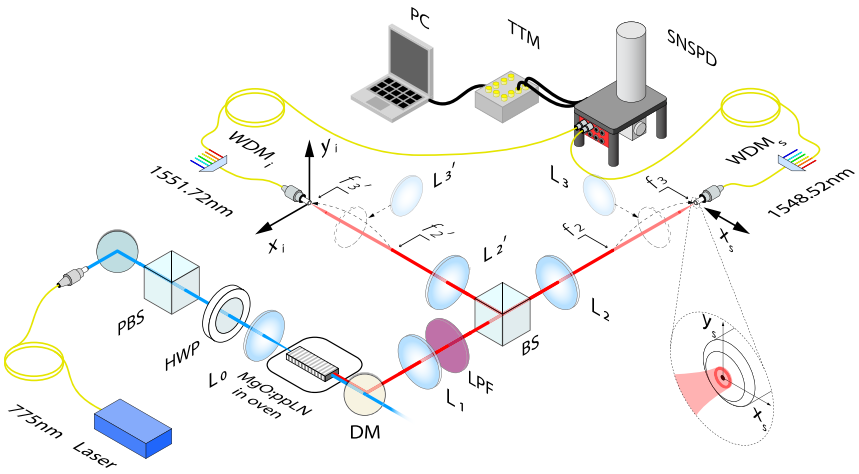

Fig. 2. Experimental setup of the type-0 phase-matched SPDC source and experimental spatial correlation measurement. A 40 mm long MgO:ppLN crystal was mounted in an oven heated to a specific temperature. It was pumped with a 775 nm cw laser (blue line) to emit SPDC photon pairs at telecommunication wavelength (red lines). The lens L_1 is located at focal distance $f_1 = 200$ mm from the center of the crystal. Two optical configurations are used to implement either near- or far-field measurements. For the near-field measurement, L_2 (L_2') was located at a distance $f_1 + f_2$ ($f_1 + f_2'$) from L1, and the fiber translation stages were placed at the focal distance $f_2 = f_2' = 150$ mm from L_2 (L_2'). For the far-field measurement, L_3 (L_3') was mounted at the focal distance $f_2 + f_3$ ($f_2' + f_3'$) from L_2 (L_2'), and the fiber translation stage was moved back at the focal distance $f_3 = f_3' = 4.5$ mm from L_3 (L_3'). In both scenarios, the photons were detected using superconducting nanowire single-photon detectors (SNSPD).

output ports of the WDMs were connected to superconducting nanowire single-photon detectors (SNSPD) with ∼80% efficiency and dark-count rates of $\sim 10^2$ Hz. Detection events were digitized and time-stamped with the aid of a time-tagging module (TTM). For each crystal temperature, we collected at the position of fibers 1 s the single and coincidence counts between signal and idler. The coincidence counts were identified when both detectors registered photons within a 200 ps time window.

C. Spectral Correlation Measurement

The second parameter in consideration is the spectral distribution of the photon pairs as a function of crystal temperature. The spectral characterization of the entangled photon-pair source was achieved via spectral separation of SPDC photons by setting up a tunable wavelength filter utilizing a reflective diffraction grating.

In this case, after lens L_1 and LPF (see Fig. 2), both signal and idler photons were coupled into an SMF and directed to the input of the tunable wavelength filter setup [see Fig. 3(a)]. After the SMF, the SPDC photons propagated towards a dispersive grating in free space. By reflection on the periodic grating, the SPDC photons were diffracted and fanned out, resulting in a spatially continuous wide signal. An SMF at the output acted as a wavelength filter of the fanned-out broad signal. The grating was positioned onto a rotation stage, and by rotation, the wavelength section that is led to the detector is altered.

The angular dispersion of the grating is 1.46 nm/mrad, which resulted in a wavelength section width of 1.25 nm that is coupled into the output SMF of the tunable wavelength filter setup. It defines the width of the wavelength bins that are detected for each rotation step. The width was determined by connecting and varying the wavelength of a tunable laser with fixed grating position resulting in Fig. 3(b). FWHM of the Gaussian-shaped

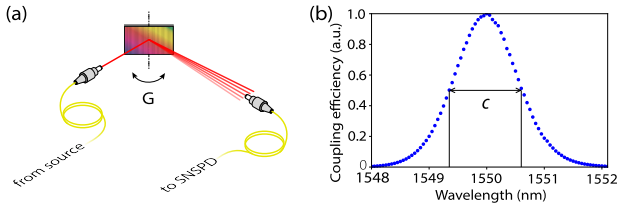

Fig. 3. (a) Experimental setup of the single-mode optical spectrometer optimized for telecommunication wavelengths. The signal of the entangled photon-pair source is coupled out from the optical fiber and led onto a blazed grating G. Subsequently, the beam is partially coupled into another single-mode fiber connected to a SNSPD. (b) The experimental curve for the coupling of a wavelength tunable laser at fixed grating position is shown. The full width at half maximum of the Gaussian-shaped curve was determined to be $C = 1.25 \pm 0.05$ nm and can be interpreted as the smallest perceptible difference in the wavelength measurable with our filter setup.

curve is C = 1.25 nm, which can be interpreted as the resolution of our spectrum analyzer.

The output SMF of the tunable wavelength filter was connected to an SNSPD channel. By step-wise rotation, a full spectrum scan of the SPDC photons was recorded. The measured property is the count rate of single photons per wavelength bin emerging from the SPDC process. Each rotation step was collected and registered with the TTM over 10 s.

4. RESULTS

A. Spatial Correlations of Type-0 Phase-Matched SPDC

1. Scan Results

We recorded the transverse momentum of the signal and idler photons by scanning its far-field planes for crystal temperatures

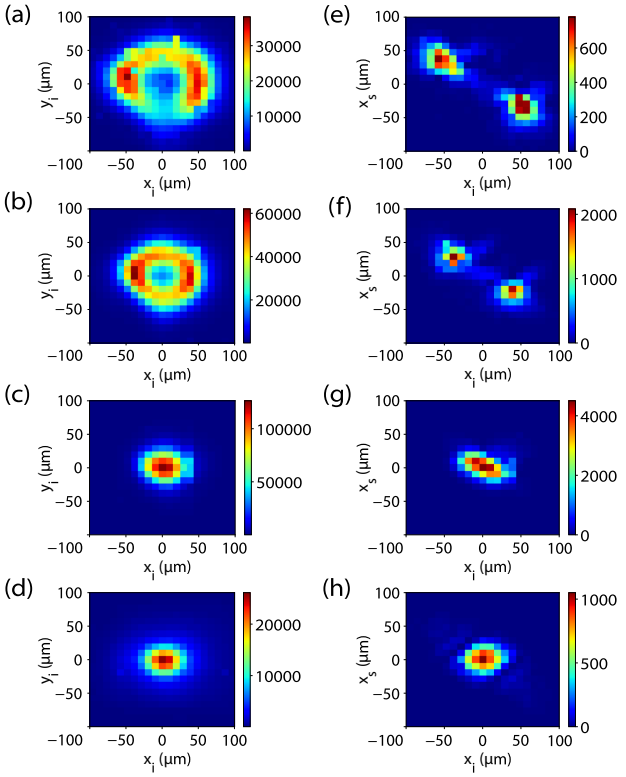

Fig. 4. Measurement of the photon spatial distribution in the far field for crystal temperatures 80°, 82°, 85°, and 88°C from top to bottom. (a)–(d) Average single counts per second for every (x_i, y_i). (e), (f) Coincident counts per second for every (x_i, x_s), when fiber positions (y_i, y_s) are at 0 μm.

ranging from 80°C to 90°C in steps of 0.5°C. To obtain the single count rate for every (x_i, y_i) position, we average the recorded counts of the idler mode over all positions of the $(x_s, y_s = 0)$ motor stage, which corresponds to an integration time of 21 s at each point. Furthermore, coincidence count rates were obtained for linear scans, i.e., $(x_i, y_i = 0)$ and $(x_s, y_s = 0)$.

Figure 4 shows the significant experimental results of the transverse plane scan in the far field over all crystal temperatures. Figures 4(a)–4(d) show the single count rates for crystal temperatures 80°, 82°, 85°, and 88°C, respectively. Figures 4(e)–4(h) depict the coincidence count rates at the same temperatures. It should be noted that the single count rates correspond to the far-field intensity profile of the photons. In the same plane, the coincidence count rates evidence the anti-correlations in transverse momenta. All experimental data are normalized to their maximum values since the fiber coupling and SPDC efficiency change for each crystal temperature.

These experimental results demonstrate that the variation in crystal temperature modifies the spatial distributions of the single and coincidence count rates in the far field. Based on the crystal temperature dependence of the phase-matching function, the collinear case is found at T = 85°C in Fig. 4(c), where the photon pairs are distributed in a small central spot with the highest coincidence count rate in Fig. 4(g). Decreasing the temperature below the collinear case, i.e., T < 85°C, yields the SPDC ring-opening in Figs. 4(a) and 4(b). The radius of the SPDC ring increases while the radial thickness of the ring decreases accordingly. In this case, the coincidence count rates are obtained by linear scans so that they are registered along the x axis in opposite emission directions, as shown in the noncollinear cases in Figs. 4(e) and 4(f). Alignment imperfections cause asymmetries in noncollinear cases when the SPDC ring expands. Figure 4(h) shows that for T > 85°C, the efficiency of the nonlinear process decreases drastically. This is due to the SPDC photon intensity distribution exhibiting as multiple secondary rings in Fig. 4(d), not just in the central spot as in the collinear case. The experimental results in Fig. 4 are qualitatively in good agreement with theoretical predictions depicted in Fig. 1(c) at the same crystal temperatures.

2. Schmidt Number Estimation

To quantify the spatial correlations of photon pairs as a function of crystal temperature, we use the Schmidt number [24]. We determine the Schmidt number of the entangled photon pairs by comparing the near- and far-field intensity distributions as introduced in [23]. (This method allows verifying entanglement by measuring one subsystem with the assumption that the bipartite state is pure. The more entangled the bipartite state, the more incoherent are its one photon states. By measuring the overall degree of coherence of one subsystem, one can then make assumptions about the overall quantum state.) This approach draws from classical coherence theory to estimate the Schmidt number K through

$$\mathrm{K} \approx \frac{1}{(2\pi)^2} \frac{\left[\int \mathrm{I_{NF}}(\mathbf{r})\mathrm{d}\mathbf{r}\right]^2}{\int \mathrm{I_{NF}^2}(\mathbf{r})\mathrm{d}\mathbf{r}} \times \frac{\left[\int \mathrm{I_{FF}}(\mathbf{q})\mathrm{d}\mathbf{q}\right]^2}{\int \mathrm{I_{FF}^2}(\mathbf{q})\mathrm{d}\mathbf{q}}, \tag{4}$$

where $\mathrm{I_{NF}}(\mathbf{r})$ is the intensity in the near field, and $\mathrm{I_{FF}}(\mathbf{q})$ is the intensity in the far field [17,25]. Here, the spatial correlations are not needed to calculate the Schmidt number [23].

The Schmidt numbers obtained from our experimental data for each crystal temperature are presented in Fig. 5. Orange dots correspond to experimental data, and error bars result from the Poissonian photon counting statistics and Gaussian error propagation. We calculated K using Eq. (4) with the theoretical description for the momentum representation given by Eq. (1), and the position representation is obtained through the Fourier transform of Eq. (1). Our experimental results are in good agreement with theory prediction considering the noncollinear and collinear propagation by varying the crystal temperature. Discrepancies between theory and experimental results can be explained by the motor mechanical backslash, temperature fluctuation during long measurements, and high sensitivity to alignment. Figure 5 shows that starting from T = 80.0°C, the value of K decreases as the temperature increases until reaching its minimum value K ≈ 18 at T = 85.5°C. This point is close to the collinear case and marks an inflection point. If the temperature rises above T > 85.5°C, K starts to increase irregularly with oscillations. The multiple SPDC rings that can be recognized in its spatial distribution increase the spatial modes of Schmidt decomposition [c.f. Eq. (1)]. Although K is higher as crystal temperature increases, the emission intensity drops rapidly. This is in contrast to T < 85.5°C, where the SPDC photons are emitted in only one ring that is opened up while the radial thickness of the ring decreases. This corroborates that the amount of

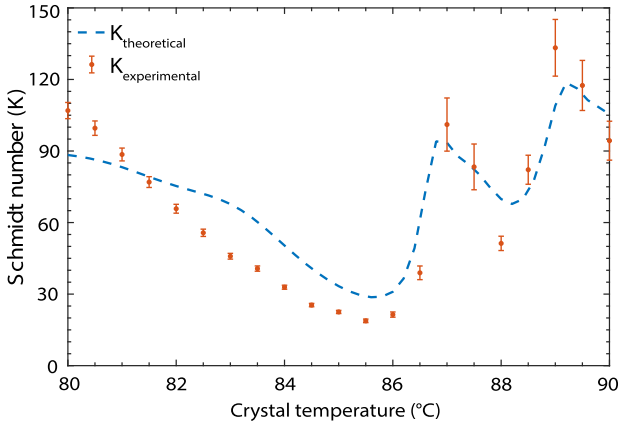

Fig. 5. Schmidt number while varying the crystal temperature for photon pairs generated with our type-0 phase-matched SPDC source. The experimental (orange dots) and theoretical (dashed blue line) Schmidt numbers were obtained from far-field and near-field intensities. The theoretical prediction was obtained by considering the SPDC photon state given by Eq. (1) and its Fourier transform.

spatial entanglement could be increased by changing the crystal temperature.

B. Temperature-Dependent Spectrum in Type-0 Phase-Matched SPDC

We measured the spectrum of the entangled photon-pair source for different crystal temperatures in a range from 82.5°C to 90°C. Figure 6 shows the theoretical and experimental normalized SPDC emission spectra at different crystal temperatures. Solid lines represent the measured spectra of the photon pairs with crystal temperatures 82.5°, 84.5°, 86.5°, 88.5°, and 90°C. Dashed lines are the theoretically predicted curves for the temperatures of the Sellmeier equation for MgO:ppLN crystals [34]. It can be observed how the SPDC spectra change from degenerate to nondegenerate wavelengths while increasing crystal temperature. Also, we can distinguish the large bandwidth characteristic for type-0 phase-matched SPDC around the degeneracy temperature ∼84°C. It is evident from Fig. 6 that the source produces degenerate photons at a spectral FWHM bandwidth of ∼40 nm. The bandwidths of the emission spectra decrease for higher temperatures.

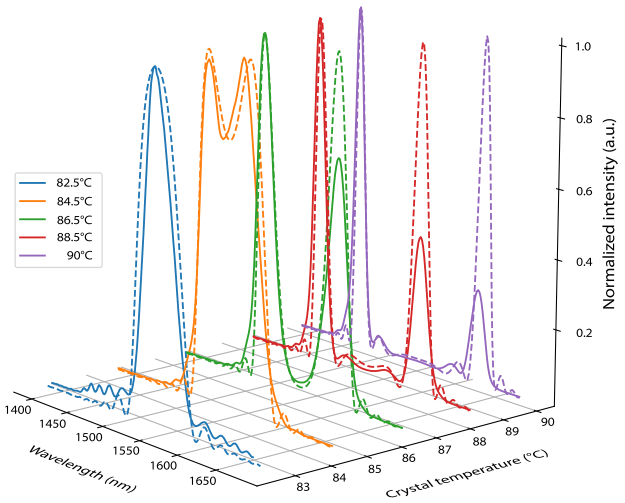

Fig. 6. Experimentally (solid lines) and theoretically calculated (dash lines) normalized emission spectra as a function of the wavelength of the type-0 entangled photon-pair source for different crystal temperatures. Data were collected with the tunable wavelength filter setup.

Although the experimental spectra are in good agreement with the theoretically estimated spectra, for nondegenerate cases, we observed some asymmetry in the recorded intensities. A plausible explanation for the observed asymmetry lies in the fact that photons with lower frequencies diverge more than its twin photons, resulting in a lower coupling efficiency into the SMF and, thus, lower count rates. Another relevant factor that could contribute to the asymmetry is the wavelength dependence of the detector efficiency since the detector has an efficiency peak at 1550 nm. For higher wavelengths, the efficiency decreases, resulting in lower detector efficiency. The fact that the asymmetry in the measured intensities increases with increasing degeneracy is consistent with both explanations.

5. CONCLUSION

We have investigated the spatial and spectral properties of photon pairs at telecommunication wavelengths generated in a type-0 phase-matched SPDC source by varying the crystal temperature. The spatial correlations were experimentally measured by a scanning approach, while spectral properties were measured with a single-mode optical spectrometer optimized for telecommunication wavelengths. We further report a good agreement between experimental results and theoretical predictions. As expected, different crystal temperatures allow significant changes from noncollinear to collinear emissions and degenerate to nondegenerate wavelengths. Crystal temperature is an accessible parameter in entangled photon-pair sources, and we have proven that it is an excellent tool to tailor them to different configurations.

Our results have practical importance in developing entanglement distribution schemes based on spatial and spectral correlations. This is particularly interesting in photon pairs at telecommunication wavelengths that can be incorporated into deployed telecommunication infrastructures and integrated with different optical fibers. Recent implementations of multicore fiber space-division [35] and entanglement distribution multiplexing [14,31] enhance the quantum channel performance in quantum communication protocols. Combined with our results, these implementations enable novel communication schemes with multiple users selecting configurations according to crystal temperature. Our characterization provides a pathway for entanglement spatial and spectral distribution in quantum networks and brings more flexibility to entangled photon-pair sources.

Funding. Horizon 2020 Framework Programme (857156); EU project Open QKD (85715); Agencia Nacional de Investigación y Desarrollo (2015-NO. 72160487, 2016-NO. 72170402).

Acknowledgment. E.A.O. and J.F. acknowledge ANID for financial support (Becas de doctorado en el extranjero "Becas Chile"). L.A. acknowledges financial support from the EU project OpenQKD.

Disclosures. The authors declare no conflicts of interest.

Data availability. Data underlying the results presented in this paper are not publicly available at this time but may be obtained from the authors upon reasonable request.

REFERENCES

1. F. Xu, X. Ma, Q. Zhang, H.-K. Lo, and J.-W. Pan, "Secure quantum key distribution with realistic devices," Rev. Mod. Phys. **92**, 025002 (2020).
2. M. Gilaberte Basset, F. Setzpfandt, F. Steinlechner, E. Beckert, T. Pertsch, and M. Gräfe, "Perspectives for applications of quantum imaging," Laser Photon. Rev. **13**, 1900097 (2019).
3. J. Fuenzalida, A. Hochrainer, G. B. Lemos, E. A. Ortega, R. Lapkiewicz, M. Lahiri, and A. Zeilinger, "Resolution of quantum imaging with undetected photons," Quantum **6**, 646 (2022).
4. H.-S. Zhong, H. Wang, Y.-H. Deng, *et al.*, "Quantum computational advantage using photons," Science **370**, 1460–1463 (2020).
5. D. Klyshko, "Scattering of light in a medium with nonlinear polarizability," Sov. Phys. JETP **28**, 522 (1969).
6. D. C. Burnham and D. L. Weinberg, "Observation of simultaneity in parametric production of optical photon pairs," Phys. Rev. Lett. **25**, 84 (1970).
7. A. Sansa Perna, E. Ortega, M. Gräfe, and F. Steinlechner, "Visible-wavelength polarization-entangled photon source for quantum communication and imaging," Appl. Phys. Lett. **120**, 074001 (2022).
8. J. D. Franson, "Bell inequality for position and time," Phys. Rev. Lett. **62**, 2205–2208 (1989).
9. G. Carvacho, J. Carine, G. Saavedra, Á. Cuevas, J. Fuenzalida, F. Toledo, M. Figueroa, A. Cabello, J.-Å. Larsson, P. Mataloni, G. Lima, and G. B. Xavier, "Postselection-loophole-free bell test over an installed optical fiber network," Phys. Rev. Lett. **115**, 030503 (2015).
10. S. Walborn, C. Monken, S. Pádua, and P. S. Ribeiro, "Spatial correlations in parametric down-conversion," Phys. Rep. **495**, 87–139 (2010).
11. A. Mair, A. Vaziri, G. Weihs, and A. Zeilinger, "Entanglement of the orbital angular momentum states of photons," Nature **412**, 313–316 (2001).
12. M. Avenhaus, M. V. Chekhova, L. A. Krivitsky, G. Leuchs, and C. Silberhorn, "Experimental verification of high spectral entanglement for pulsed waveguided spontaneous parametric down-conversion," Phys. Rev. A **79**, 043836 (2009).
13. J. Chen, G. Wu, L. Xu, X. Gu, E. Wu, and H. Zeng, "Stable quantum key distribution with active polarization control based on time-division multiplexing," New J. Phys. **11**, 065004 (2009).
14. J. Pseiner, L. Achatz, L. Bulla, M. Bohmann, and R. Ursin, "Experimental wavelength-multiplexed entanglement-based quantum cryptography," Quantum Sci. Technol. **6**, 035013 (2021).
15. B. J. Puttnam, G. Rademacher, and R. S. Luís, "Space-division multiplexing for optical fiber communications," Optica **8**, 1186–1203 (2021).
16. M. Erhard, M. Krenn, and A. Zeilinger, "Advances in high-dimensional quantum entanglement," Nat. Rev. Phys. **2**, 365–381 (2020).
17. L. Achatz, E. A. Ortega, K. Dovzhik, R. F. Shiozaki, J. Fuenzalida, S. Wengerowsky, M. Bohmann, and R. Ursin, "Certifying position-momentum entanglement at telecommunication wavelengths," Phys. Scripta **97**, 015101 (2022).
18. A. Anwar, C. Perumangatt, F. Steinlechner, T. Jennewein, and A. Ling, "Entangled photon-pair sources based on three-wave mixing in bulk crystals," Rev. Sci. Instrum. **92**, 041101 (2021).
19. M. Fejer, G. Magel, D. Jundt, and R. Byer, "Quasi-phase-matched second harmonic generation: tuning and tolerances," IEEE J. Quantum Electron. **28**, 2631–2654 (1992).
20. H. Di Lorenzo Pires, F. M. G. J. Coppens, and M. P. van Exter, "Type-i spontaneous parametric down-conversion with a strongly focused pump," Phys. Rev. A **83**, 033837 (2011).
21. W. P. Grice, R. S. Bennink, D. S. Goodman, and A. T. Ryan, "Spatial entanglement and optimal single-mode coupling," Phys. Rev. A **83**, 023810 (2011).
22. R. Ramírez-Alarcón, H. Cruz-Ramírez, and A. B. U'Ren, "Effects of crystal length on the angular spectrum of spontaneous parametric downconversion photon pairs," Laser Phys. **23**, 055204 (2013).
23. H. Di Lorenzo Pires, C. H. Monken, and M. P. van Exter, "Direct measurement of transverse-mode entanglement in two-photon states," Phys. Rev. A **80**, 022307 (2009).
24. C. K. Law and J. H. Eberly, "Analysis and interpretation of high transverse entanglement in optical parametric down conversion," Phys. Rev. Lett. **92**, 127903 (2004).
25. H. Di Lorenzo Pires and M. P. van Exter, "Near-field correlations in the two-photon field," Phys. Rev. A **80**, 053820 (2009).
26. H. D. L. Pires and M. van Exter, "Observation of near-field correlations in spontaneous parametric down-conversion," Phys. Rev. A **79**, 041801 (2009).
27. F. Steinlechner, M. Gilaberte, M. Jofre, T. Scheidl, J. P. Torres, V. Pruneri, and R. Ursin, "Efficient heralding of polarization-entangled photons from type-0 and type-ii spontaneous parametric down-conversion in periodically poled $KTiOPO_4$," J. Opt. Soc. Am. B **31**, 2068–2076 (2014).
28. A. K. Ghatak and K. Thyagarajan, "Optical waveguides and fibers," in *Fundamentals of Photonics* (2008), Chap. 7.
29. S. Wengerowsky, S. K. Joshi, F. Steinlechner, J. R. Zichi, S. M. Dobrovolskiy, R. van der Molen, J. W. N. Los, V. Zwiller, M. A. M. Versteegh, A. Mura, D. Calonico, M. Inguscio, H. Hübel, L. Bo, T. Schneidl, A. Zeilinger, A. Xuereb, and R. Ursin, "Entanglement distribution over a 96-km-long submarine optical fiber," Proc. Natl. Acad. Sci. USA **116**, 6684–6688 (2019).
30. S. P. Neumann, A. Buchner, L. Bulla, M. Bohmann, and R. Ursin, "Continuous entanglement distribution over a transnational 248km fiber link," Nat. Commun. **13**, 6134 (2022).
31. S. K. Joshi, D. Aktas, S. Wengerowsky, M. Lončarić, S. P. Neumann, B. Liu, T. Scheidl, G. C. Lorenzo, Ž. Samec, L. Kling, A. Qiu, M. Razavi, M. Stipčević, J. G. Rarity, and R. Ursin, "A trusted node–free eight-user metropolitan quantum communication network," Sci. Adv. **6**, eaba0959 (2020).
32. A. Pickston, F. Graffitti, P. Barrow, C. L. Morrison, J. Ho, A. M. Brańczyk, and A. Fedrizzi, "Optimised domain-engineered crystals for pure telecom photon sources," Opt. Express **29**, 6991–7002 (2021).
33. F. Kaneda, J. Oikawa, M. Yabuno, F. China, S. Miki, H. Terai, Y. Mitsumori, and K. Edamatsu, "Spectral characterization of photon-pair sources via classical sum-frequency generation," Opt. Express **28**, 38993–39004 (2020).
34. O. Gayer, Z. Sacks, E. Galun, and A. Arie, "Temperature and wavelength dependent refractive index equations for MgO-doped congruent and stoichiometric $LiNbO_3$," Appl. Phys. B **91**, 343–348 (2008).
35. E. A. Ortega, K. Dovzhik, J. Fuenzalida, S. Wengerowsky, J. C. Alvarado-Zacarias, R. F. Shiozaki, R. Amezcua-Correa, M. Bohmann, and R. Ursin, "Experimental space-division multiplexed polarization-entanglement distribution through 12 paths of a multicore fiber," PRX Quantum **2**, 040356 (2021).

3.2 Simultaneous transmission of hyper-entanglement in 3 degrees of freedom through a multicore fiber

For this publication we combined the technique of space division multiplexing through a multi-core fiber with hyper-entanglement in energy-time and polarization. We furthermore verified simultaneous transmission of a high-dimensional hyper-entangled state in the degrees of energy-time, polarization and path through a multi-core fiber for the first time, to the best of our knowledge.

I contributed by planning the experiment with Rupert Ursin and Sebastian Ecker. I built the experimental setup for analyzing energy-time entanglement together with Lukas Bulla and Sebastian Ecker and helped Michael Bartokos in building the module for analyzing path entanglement. Furthermore, I conducted all measurements with help from Lukas Bulla and Michael Bartokos and analyzed the obtained data for energy-time and polarization entanglement. Entanglement in the path degree of freedom was analyzed together with Marcus Huber. I wrote the paper together with help from Sebastian Ecker and Marcus Huber.

npj | quantum information www.nature.com/npjqi

ARTICLE OPEN

Check for updates

Simultaneous transmission of hyper-entanglement in three degrees of freedom through a multicore fiber

Lukas Achatz[1,2]✉, Lukas Bulla[1,2], Sebastian Ecker[1,2], Evelyn A. Ortega[1,2], Michael Bartokos[1], Juan Carlos Alvarado-Zacarias[3], Rodrigo Amezcua-Correa[3], Martin Bohmann[1,2], Rupert Ursin[1,2] and Marcus Huber[1,2]✉

Entanglement distribution is at the heart of most quantum communication protocols. Inevitable loss of photons along quantum channels is a major obstacle for distributing entangled photons over long distances, as the no-cloning theorem forbids the information to simply be amplified along the way as is done in classical communication. It is therefore desirable for every successfully transmitted photon pair to carry as much entanglement as possible. Spontaneous parametric down-conversion (SPDC) creates photons entangled in multiple high-dimensional degrees of freedom simultaneously, often referred to as hyper-entanglement. In this work, we use a multicore fiber (MCF) to show that energy-time and polarization degrees of freedom can simultaneously be transmitted in multiple fiber cores, even maintaining path entanglement across the cores. We verify a fidelity to the ideal Bell state of at least 95% in all degrees of freedom. Furthermore, because the entangled photons are created with a center wavelength of 1560 nm, our approach can readily be integrated into modern telecommunication infrastructure, thus paving the way for high-rate quantum key distribution and many other entanglement-based quantum communication protocols.

npj Quantum Information (2023)9:45 ; https://doi.org/10.1038/s41534-023-00700-0

INTRODUCTION

Quantum-information science has seen rapid progress in recent years. Quantum entanglement is one of the driving forces behind quantum-information processing, and its generation and distribution are therefore of utmost importance. Among many other applications, quantum key distribution (QKD)[1–3], quantum computation[4,5] and superdense coding[6] heavily rely on the presence of entanglement. A key feature of photons is that they can be simultaneously entangled in multiple of their degrees of freedom (DOF), thus creating hyper-entangled states[7–11]. By exploiting hyper-entanglement one can greatly increase the dimensionality of the resulting Hilbert space, effectively increasing the quantum information per transmitted photon[12].

Another way of increasing the transmission rate has been a standard in the classical telecommunication industry for quite some time, namely multiplexing. Here, many signals are combined (multiplexed) into one transmission channel and separated (demultiplexed) at the receiver site. In the quantum regime, multiplexing can be used to overcome the timing limitations imposed by the timing precision and dead time in the detection module, and hence significantly increase the secure key rate[13].

In recent years, the interest in multiplexing of entangled photons in different DOFs has grown[13–17]. Achieving coherence and entanglement in the multiplexed DOFs offers another exciting avenue for high-rate quantum communication: directly encoding in energy-time or spatial DOFs also allows for high-dimensional protocols, which offer increased capacity in high-dimensional QKD protocols[18–20] as well as improved noise resilience[21–23], essentially only limited by the spatial or temporal resolution of the detection scheme.

In this article, we present an experiment separated into two parts, in which we prove successful transmission of spatial, energy-time as well as polarization entanglement through more than 400 m of multicore fiber (MCF). First, we certified hyper-entanglement in polarization and energy-time and combined it with the technique of space-division multiplexing. The entangled photons were spatially multiplexed using a multicore fiber, which consists of 19 single-mode fibers inside a single cladding, connected to a fan-in/fan-out device. We verified entanglement for four randomly chosen opposite core pairs of the MCF and achieved visibilities up to 94% in both energy-time and polarization.

In a second step, we verified the transmission of path entanglement through the MCF by non-locally interfering two neighboring core pairs on two separate beamsplitters. By varying the phase between the photon pairs, visibility fringes with a visibility up to 96% were measured. As the core pairs are identical, we can conclude that the MCF is indeed capable of transmitting hyper-entanglement in all DOFs faithfully.

The presented approach opens up the possibility of using a single source for generating hyper-entangled photons and efficiently distribute them through a MCF. Furthermore, because the wavelength of the entangled photons is centered around 1560 nm, the presented approach can be readily integrated into existing telecommunication infrastructure, thus paving the way for higher transmission rates in existing and future QKD protocols as well as other quantum-information applications. To the best of our knowledge, this is the first demonstration of transmitting a hyper-entangled state in three DOFs through a multicore fiber.

RESULTS

Energy-time and polarization entanglement analysis

In the first part of the experiment, we simultaneously studied the entanglement in the energy-time and polarization domain. The experimental setup consists of a high-dimensional photon pair source and different analysis setups both at Alice's and Bob's site

[1]Institute for Quantum Optics and Quantum Information - IQOQI Vienna, Austrian Academy of Sciences, Boltzmanngasse 3, 1090 Vienna, Austria. [2]Vienna Center for Quantum Science and Technology (VCQ), Vienna, Austria. [3]CREOL, The University of Central Florida, Orlando, FL 32816, USA. ✉email: achatz.lukas@gmail.com; marcus.huber@oeaw.ac.at

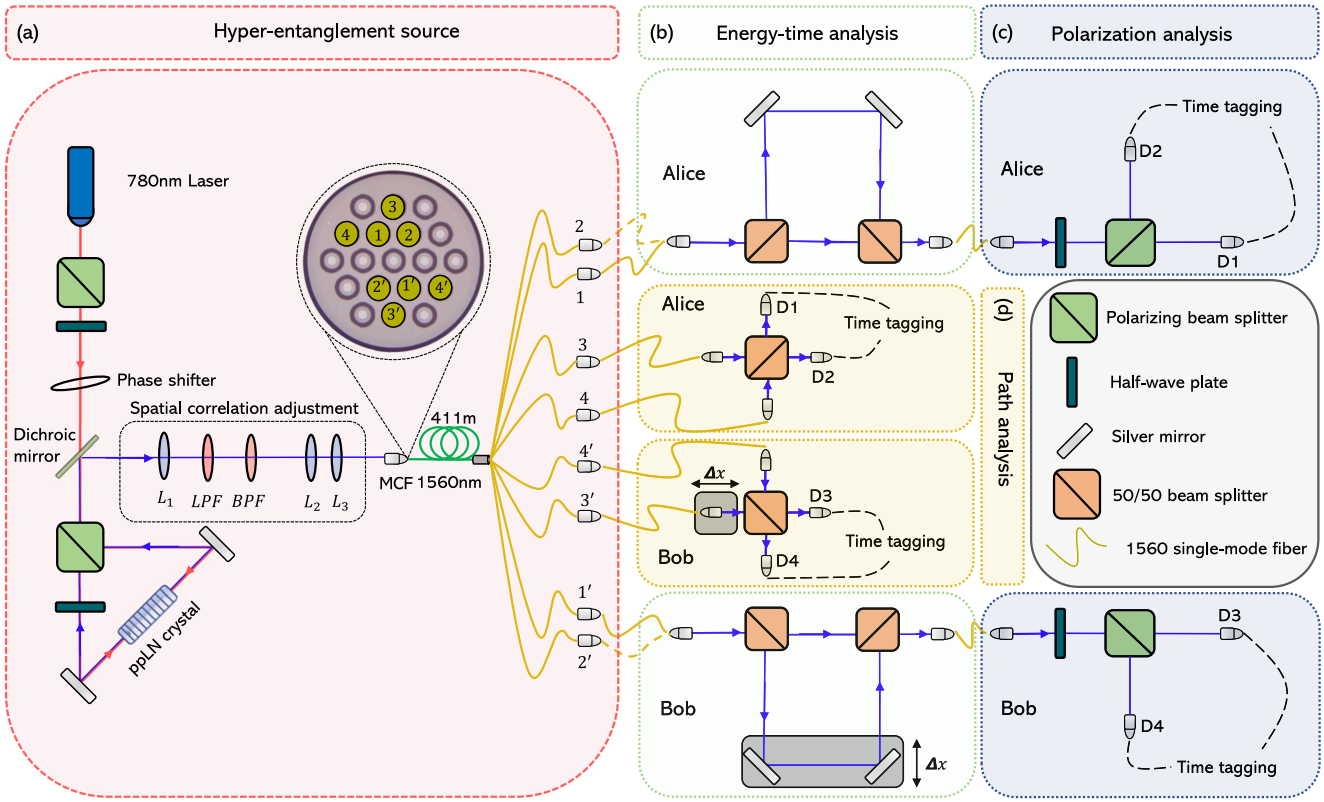

Fig. 1 Experimental setup. a Hyper-entanglement source: A MgO:ppLN non-linear crystal is bi-directionally pumped in a Sagnac configuration by a continuous wave laser at 780.24 nm. Because of this special configuration a hyper-entangled state in polarization, energy-time and position-momentum with a center wavelength of 1560.48 nm is produced. A dichroic mirror (DM) splits the pump light and the SPDC signal. Through the use of a lens configuration the momentum anti-correlations of the entangled photons are imaged onto the front facet of a 19 core MCF. A longpass filter further filters out the pump light while a bandpass filter with a FWHM of 1560 ± 2.4 nm selects only the photons centered around the center wavelength. This filtering procedure greatly increases the momentum anti-correlations, since a filtering in wavelength is directly proportional to a filtering on the **k**-vectors of the photons. Since the opening angle of the emission cone is highly dependent on the crystals' temperature[30] a temperature of 80.5 °C was chosen for the inner ring (cores 1, 1′, 2, 2′) while for the outer ring (cores 3, 3′, 4, 4′) the temperature was 77.5 °C. **b** Energy-time analysis: Two opposite core pairs (either 1 and 1′ or 2 and 2′) are coupled to two separate Franson interferometers. The mirrors of the long arm of Bob's interferometer are mounted on a translation stage. By moving the stage one can vary the phase ϕ in Eq. (1) between the long and short arms. **c** Polarization analysis: Consisting of a HWP and a PBS. By rotating the HWPs one can specify the measurement basis, either HV or DA. **d** Path analysis: Two neighboring core pairs non-locally interfere on two separate 50/50 BS. Through the thusly created path indistinguishability a superposition basis is generated. A key aspect in achieving this is ensuring equal path length differences of all cores within the coherence length of the entangled photons. By varying the distance of one core to one BS with a translation stage the phase θ in Eq. (2) is tuned. In order to compensate for polarization drifts in the fiber a PBS was inserted before every input port of the BS, which for simplicity is not shown in the figure. All optical elements in (**b**), (**c**) and (**d**) are bulk optics.

(see Fig. 1). The entangled photon pairs were produced via spontaneous parametric down-conversion (SPDC)[24].

Because of momentum conversation in the SPDC process, the signal and idler photons are emitted with opposite transverse momenta, resulting in $\mathbf{q}_s = -\mathbf{q}_i$, where $\mathbf{q}_s$ ($\mathbf{q}_i$) refers to the transverse momentum of the signal (idler) photon. Entanglement in position-momentum for this particular source has already been shown in a previous work[25]. By utilizing a lens system in the far-field plane of the crystal, we imaged the momentum correlations onto the front facet of a 411-m-long MCF. Our MCF consists of 19 single-mode fibers (SMF) in a hexagonal pattern (see Fig. 1). Because of the anti-correlation in momentum, the partner photon of a collected photon in any core can be found in the diametrically opposite core. Collecting the photons in opposing cores enables the separation of the two entangled photons despite its wavelength-degenerate spectrum. For a more detailed description of the lens setup and MCF the reader is referred to[15].

Entanglement in the energy-time DOF arises from energy conservation in the SPDC process. After the fan-out of the MCF, the entangled photon pairs are transmitted to two imbalanced Mach–Zehnder interferometers, one for each user, which constitutes a Franson interferometer[26].

The created hyper-entangled wave function in each core is close to

$$\left|\Psi_{E,P}\right\rangle = \frac{1}{2}\left[\left(|S\rangle|S\rangle + e^{i\phi}|L\rangle|L\rangle\right) \otimes \left(|H\rangle|H\rangle + |V\rangle|V\rangle\right)\right] \quad (1)$$

where $|S\rangle$ and $|L\rangle$ refer to short and long paths and $|H\rangle$ and $|V\rangle$ refer to horizontal and vertical polarization. The phase ϕ can be adjusted via a piezo actuator in the long arm of Bob's interferometer.

After the energy-time analysis the photons are transmitted to a polarization analysis module, consisting of a half-wave plate and a polarizing beamsplitter. They are subsequently measured by superconducting nanowire single-photon detectors (SNSPD) with an efficiency of ~80% and dark-count rates of ~10^2 Hz.

The results of the visibility fringe measurements for different polarization settings and cores are shown in Tables 1, 2.

As can be seen in Tables 1, 2 all visibilities are greater than 81%, which is the limit for QKD protocols for which a key can be extracted.

Table 1. Obtained visibilities from scanning the long arm ob Bob's interferometer for the core combination 1-1′.

Detector combination	Time visibility [%]
HH	86.6 ± 3.1
VV	94.2 ± 1.6
DD	89.5 ± 2.7
AA	90.6 ± 2.1

HH and VV correspond to measurements in the HV basis while DD and AA correspond to measurements in the DA basis.

Table 2. Obtained visibilities from scanning the long arm ob Bob's interferometer for the core combination 2-2′.

Detector combination	Time visibility [%]
HH	90.1 ± 2.9
VV	89.5 ± 2.1
DD	88.7 ± 2.7
AA	94.1 ± 1.8

HH and VV correspond to measurements in the HV basis while DD and AA correspond to measurements in the DA basis.

Path entanglement analysis

As a second step the path entanglement transmitted through the MCF was analyzed. The experimental setup for the source is identical to the one explained in Sec. Energy-time and polarization entanglement analysis. In order to analyze path entanglement two core pairs in the outer ring of the MCF were non-locally interfered on two BS, as is shown in Fig. 1. By guaranteeing an equal distance from the front facet of the MCF to the interfering point on the BS a superposition basis is created[27]. The wave function projected on these two cores would ideally read as

$$|\psi_S\rangle = \frac{1}{\sqrt{2}}\left(|3\rangle|3'\rangle - e^{i\theta}|4\rangle|4'\rangle\right) \quad (2)$$

where $|3\rangle$, $|3'\rangle$, $|4\rangle$ and $|4'\rangle$ refer to the different cores of the MCF. By adjusting the path length difference of one core with a piezo electrical actuator, effectively varying the phase θ, visibility fringes between different output ports of the BS are observed.

Before we move on to results let us briefly define the overall target state, which we would expect to feed into the MCF and hope to certify at the output:

$$|\Psi_T\rangle := \tfrac{1}{4}(|11'\rangle + |22'\rangle + |33'\rangle + |44'\rangle) \otimes (|SS\rangle + |LL\rangle) \otimes (|HH\rangle + |VV\rangle) \quad (3)$$

The obtained results are shown in Fig. 2. The calculated visibilities are listed in Table 3. As can be seen visibilities as high as 97.6% were achieved, demonstrating a high degree of entanglement.

In Fig. 2 a slight offset between different detector combinations is noticeable. This most likely stems from a slight length-offset between the non-interfering core pairs. This fact, however, does not compromise the visibility results.

The visibility implies a verified off-diagonal element in the path basis of $|\langle 33'|\rho|44'\rangle| = 0.24$[28]. In this non-adversarial scenario one can safely assume that this value is representative for all the elements $|\langle ii'|\rho|jj'\rangle|$ (when utilizing a multicore fiber in a real-world scenario, it is of course of utmost importance to experimentally verify the equivalency of all cores). This, together with the coincidences across the cores, i.e. the measured diagonal

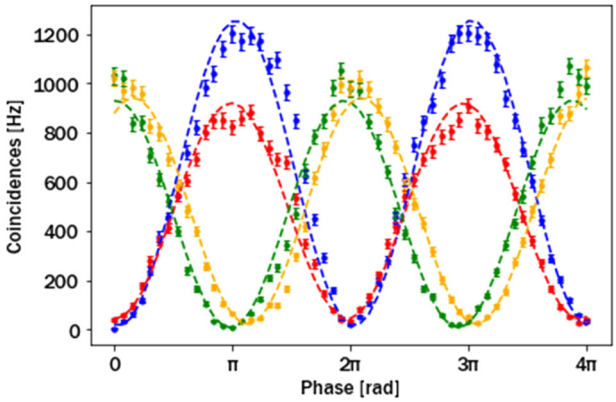

Fig. 2 Measured path visibility fringes between different detector combinations with an integration time of 1s. The detector combinations are the following: blue D1/D3, red D2/D4, green D1/D4 and yellow D2/D3. For the errors we assumed Poissonian statistics. The difference in the absolute coincidence counts is most likely due to different losses for each channel, such as coupling and detection efficiencies at the SNSPDs.

Table 3. Obtained visibilities from varying the length of one core.

Phase	Path visibility [%]
0	97.6 ± 0.6
π	95.8 ± 0.9

The two points correspond to visibilities for different measurement bases, which we took to define $\sigma_x \otimes \sigma_x$ and $\sigma_y \otimes \sigma_y$.

basis elements in path basis, gives a final fidelity with the maximally path entangled state of $F_{\text{path}} = 0.953$, which is well above the bound for qutrit entanglement of 0.75, thus proving a Schmidt number of four or in other words genuine four-dimensional entanglement.

DISCUSSION

The presented approach offers multiple advantages for applications which need to be highlighted. While we connected separate measurement setups to verify entanglement in different DOFs, the source (except for crystal temperature) and the fiber remained unperturbed, proving simultaneous presence of all hyper-entangled DOFs after MCF transmission. First, we demonstrated the successful transmission of a spatially multiplexed polarization and energy-time hyper-entangled state through the inner cores of the 411-m-long MCF. By using the technique of multiplexing, timing limitations in present detector systems are circumvented and the secure key rate is increased[13]. Since the photons' momenta are anti-correlated, one can distribute multiple pairs to different users by using opposing cores of a multicore fiber. Furthermore by using two MCFs, one for each user, one can use the intrinsic phase-stability of MCFs[29] for efficiently distributing high-dimensional entanglement. One can also use the spatial entanglement across cores to maximize rates for a single pair of users. In this context, and as a second step, we verified entanglement in the path DOF by non-locally interfering two opposite core pairs of the outer ring of the MCF on two beamsplitters. We achieved visibilities as high as 97%, underlining the high-dimensional nature of the path entanglement. Note that the temperatures for the first and second measurement differed by 3 °C, maximizing the count rates either in the inner or outer rings of the MCF. This is because the spatial crosstalk between different cores is reduced by about 1% in the outer ring, as is

shown in[30]. When combining all measurement setups sequentially, the coincidence count rates were in the order of 20 Hz. Since no active phase stabilization was used, the phase fluctuations of all setups were rendering a measurement impossible. In a real-world scenario one could use active spatial phase-stabilization[31] and active polarization stabilization[32] for a continuous QKD-protocol. Another possible application is superdense coding[33] which has recently been realized with qu-quarts in Ref. [34] as well as superdense teleportation[35] and single-copy entanglement distillation[36]. In recent years, another interesting possibility has been studied, namely the transmission of high-dimensional hybrid orbital angular momentum (OAM) and polarization states, both for prepare and measure[37] as well as entanglement-based QKD schemes[38]. By utilizing the high-dimensional OAM modes of the photons, reliable QKD schemes with a high secure key rate can be implemented, as is shown in Ref. [39]. To further improve the transmission rate in future applications, one could utilize few-mode MCF for the distribution of high-dimensional entanglement, as is shown in Ref. [40]. For a thorough review on previous works in the field of transmission of OAM through fibers, the reader is referred to Ref. [41].

Since our entanglement source naturally produces wavelength-correlated photon pairs, the presented approach offers high scalability by additionally integrating dense wavelength-division multiplexing, as is done for example in Ref. [14]. The used wavelength of 1560 nm makes our approach readily integrable into current telecommunication infrastructure, thus paving the way for highly efficient quantum-information protocols over deployed fiber networks.

METHODS

Source design

By pumping a type-0 non-linear SPDC crystal in a Sagnac configuration[42] with a CW-laser at a wavelength of 780.24 nm, polarization-entangled photons with a center wavelength of 1560.48 nm are produced. The created photons are inherently entangled in the energy-time and position-momentum domain. Because of the special Sagnac configuration the produced photons also exhibit polarization entanglement. The photon-pair spectrum is filtered by a ±2.4 nm (FWHM) bandpass filter to select degenerate photons. By decreasing the spectral width of the photons, the momentum correlations are greatly enhanced in return, which limits the crosstalk between different cores inside the MCF[15]. While SPDC might be the most commonly used way of generating photonic entanglement, it has several limitations which are worth mentioning, such as the low efficiency of roughly 10^{-5} pairs per pump photon[43] as well as the probability to generate multi-pairs.

Franson Interferometer

At the first beamsplitter of the interferometer, the photons are either transmitted into the short arm or reflected into the long arm. The propagation difference between the long and the short arm amounts to a delay of 1.2 ns. They are then recombined at a second beamsplitter. The cases where both photons take the same paths in both Mach-Zehnder interferometers (either short-short or long-long) are temporally indistinguishable. Therefore, post-selection on the coincidences reveals non-local interference[44]. It is important to note that the path length difference ΔL between the short and long arms of both interferometers must be smaller than the coherence time τ_{cc} of the entangled photons. Furthermore, the path length difference has to be greater than the detector's timing jitter, which is about 15 ps for SNSPDs. Due to polarization mode dispersion inside the MCF a half-wave plate at 0° was inserted in the long arm of Bob's interferometer. This acts as a phase retarder and compensates for the phase difference of one photon due to transmission inside the MCF. On average, the single-photon count rate was about 125 kHz and the coincidence count rate was about 300 Hz. Accidental coincidences in the order of 5 Hz were subtracted from all coincidence counts. The low heralding efficiency, i.e. coincidence-to-single-ratio, is a result of the low-efficiency coupling of the SPDC light into the MCF. A micro-lens array[45] could greatly increase the heralding efficiency of our source.

Path interferometer

In order to create a superposition basis for the Path DOF one has to ensure an equal distance from the front facet of the MCF to the interfering point on the BS[27]. Additionally, the path length difference between all cores has to be smaller than the coherence length of the entangled photons. Since only photons with the same polarization state interfere, a PBS was inserted in front of the BS. By this measure polarization drifts in one core will not affect the path visibility but rather just reduce the heralding. Accidental coincidences in the order of 10 Hz were subtracted from all coincidence counts.

Energy-time and polarization visibility measurements

In order to verify the transmission of hyper-entanglement through the MCF, at first, both HWPs at the polarization modules were set to H, inducing no phase shift on the polarization state of the photons, thus corresponding to a measurement in the HV-basis. To analyze the hyper-entangled state in its entirety, the long arm of Bob's interferometer was scanned, effectively varying the phase ϕ in the first part of Eq. (1). The obtained visibility fringes are shown in Fig. 3. At every step Δx of Bob's interferometer the integration time was 30*s* and the coincidence counts for the detector combinations HH (D1/D3), VV (D2/D4), HV (D1/D4) and VH (D2/D3) were recorded. Thereby a polarization visibility at every Δx is obtained. The polarization visibilities are shown in Fig. 4, where the green area represents a visibility of higher than 81%. Since a $|\Phi^+\rangle$ Bell state was produced, correlations only arise between HH (DD) and VV (AA), while there are no correlations between HV (DA) and VH (AD).

The polarization visibility is calculated with

$$V_{\mathrm{pol}} = \frac{\mathrm{CC}_{HH} + \mathrm{CC}_{VV} - \mathrm{CC}_{HV} - \mathrm{CC}_{VH}}{\mathrm{CC}_{HH} + \mathrm{CC}_{VV} + \mathrm{CC}_{HV} + \mathrm{CC}_{VH}}, \tag{4}$$

where $\mathrm{CC}_{\mathrm{signal,idler}}$ corresponds to the coincidence counts for each output port of the polarizing beamsplitter. In order to calculate the visibilities in the energy-time DOF, the obtained fringes were fitted with a sine function and calculated with

$$V_{\mathrm{time}} = \frac{\mathrm{CC}_{\mathrm{max}} - \mathrm{CC}_{\mathrm{min}}}{\mathrm{CC}_{\mathrm{max}} + \mathrm{CC}_{\mathrm{min}}}. \tag{5}$$

The same procedure was repeated for a measurement in the DA basis, meaning that both HWPs in the polarization modules were rotated by 22.5°.

Path visibility measurements

In order to verify the transmission of path entanglement through the MCF the path lengths of all cores have to be identical in the order of the coherence length of the photons. By varying the distance to the BS of one core via a piezo electrical actuator the phase θ in Eq. (2) is tuned. Coincidence counts between all four detector combinations were recorded with an integration time of 1 s.

In order to obtain the visibilities the obtained fringes were fitted with a sine function and subsequently calculated with

$$V_{\mathrm{path}} = \frac{\mathrm{CC}_{\mathrm{max}} - \mathrm{CC}_{\mathrm{min}}}{\mathrm{CC}_{\mathrm{max}} + \mathrm{CC}_{\mathrm{min}}} \tag{6}$$

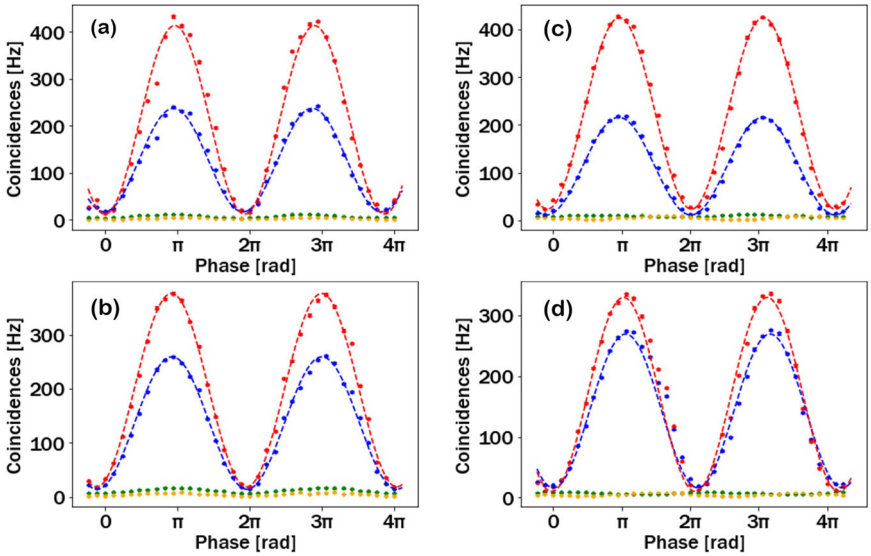

Fig. 3 Measured time visibility fringes by varying Bob's phase. Blue represents the coincidences for HH (DD), red for VV (AA), green for HV (DA) and yellow for VH (AD). **a** Core pair 1-1′ HV Basis, (**b**) Core pair 1-1′ DA Basis, (**c**) Core pair 2-2′ HV Basis, (**d**) Core pair 2-2′ DA Basis. For each data point the integration time was 30 s. We assumed Poissonian statistics, note that the errors are smaller than the data points.

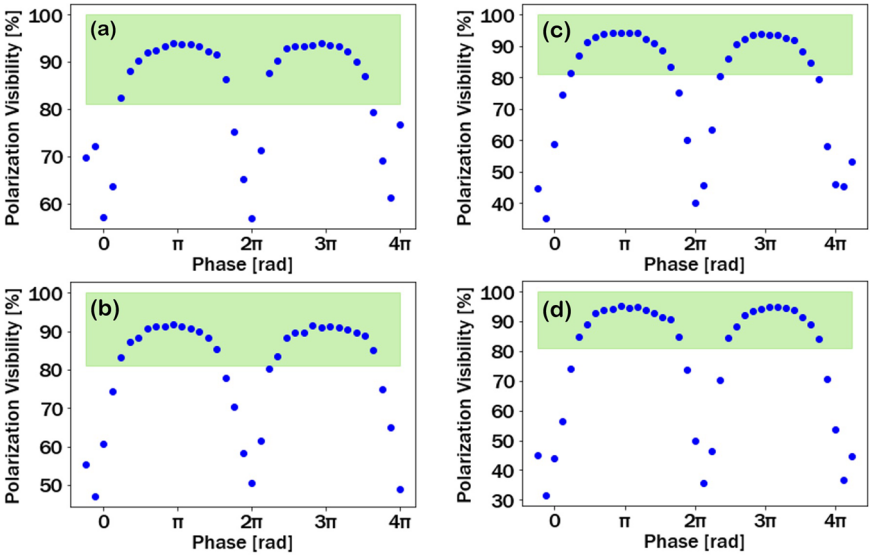

Fig. 4 Measured polarization visibility fringes by varying Bob's phase. The green area represents a visibility of greater than 81%, representing the limit for QKD protocols. **a** Core pair 1-1′ HV Basis, **b** Core pair 1-1′ DA Basis, (**c**) Core pair 2-2's HV Basis, (**d**) Core pair 2-2′ DA Basis. At multiples of 2π the polarization visibility drops. This stems from the fact that destructive interference for the coincidences occurs, thus fewer coincidences are measured. For each data point the integration time was 30 s. We assumed Poissonian statistics, note that the errors are smaller than the data points.

DATA AVAILABILITY

The data are available from the author at reasonable request.

Received: 4 November 2022; Accepted: 15 March 2023;
Published online: 05 May 2023

REFERENCES

1. Ekert, A. K. Quantum cryptography based on bell's theorem. *Phys. Rev. Lett.* **67**, 661–663 (1991).
2. Gisin, N., Ribordy, G., Tittel, W. & Zbinden, H. Quantum cryptography. *Rev. Mod. Phys.* **74**, 145–195 (2002).
3. Xu, F., Ma, X., Zhang, Q., Lo, H.-K. & Pan, J.-W. Secure quantum key distribution with realistic devices. *Rev. Mod. Phys.* **92**, 025002 (2020).
4. Steane, A. Quantum computing. *Rep. Prog. Phys.* **61**, 117–173 (1998).
5. Barz, S. et al. Demonstration of blind quantum computing. *Science* **335**, 303–308 (2012).
6. Wang, C., Deng, F.-G., Li, Y.-S., Liu, X.-S. & Long, G. L. Quantum secure direct communication with high-dimension quantum superdense coding. *Phys. Rev. A* **71**, 044305 (2005).
7. Kwiat, P. G. Hyper-entangled states. *J. Mod. Opt.* **44**, 2173–2184 (1997).
8. Barreiro, J. T., Langford, N. K., Peters, N. A. & Kwiat, P. G. Generation of hyper-entangled photon pairs. *Phys. Rev. Lett.* **95**, 260501 (2005).
9. Suo, J., Dong, S., Zhang, W., Huang, Y. & Peng, J. Generation of hyper-entanglement on polarization and energy-time based on a silicon micro-ring cavity. *Opt. Express* **23**, 3985–3995 (2015).

10. Deng, F.-G., Ren, B.-C. & Li, X.-H. Quantum hyperentanglement and its applications in quantum information processing. *Sci. Bull.* **62**, 46–68 (2017).
11. Chapman, J. C., Lim, C. C. W. & Kwiat, P. G. Hyperentangled time-bin and polarization quantum key distribution. Phys. Rev. **18**, 044027 (2019).
12. Kwiat, P. G. & Graham, T. in *Frontiers in Optics 2011/Laser Science XXVII*, LTuI1 (Optica Publishing Group, 2011).
13. Pseiner, J., Achatz, L., Bulla, L., Bohmann, M. & Ursin, R. Experimental wavelength-multiplexed entanglement-based quantum cryptography. *Quantum Sci. Technol.* **6**, 035013 (2021).
14. Vergyris, P. et al. Fibre based hyperentanglement generation for dense wavelength division multiplexing. *Quantum Sci. Technol.* **4**, 045007 (2019).
15. Ortega, E. A. et al. Experimental space-division multiplexed polarization-entanglement distribution through 12 paths of a multicore fiber. *PRX Quantum* **2**, 040356 (2021).
16. Wengerowsky, S., Joshi, S. K., Steinlechner, F., Hübel, H. & Ursin, R. An entanglement-based wavelength-multiplexed quantum communication network. *Nature* **564**, 225–228 (2018).
17. Kim, J.-H., Chae, J.-W., Jeong, Y.-C. & Kim, Y.-H. Quantum communication with time-bin entanglement over a wavelength-multiplexed fiber network. *APL Photonics* **7**, 016106 (2022).
18. Bechmann-Pasquinucci, H. & Tittel, W. Quantum cryptography using larger alphabets. *Phys. Rev. A* **61**, 062308 (2000).
19. Ali-Khan, I., Broadbent, C. J. & Howell, J. C. Large-alphabet quantum key distribution using energy-time entangled bipartite states. *Phys. Rev. Lett.* **98**, 060503 (2007).
20. Martin, A. et al. Quantifying photonic high-dimensional entanglement. *Phys. Rev. Lett.* **118**, 110501 (2017).
21. Ecker, S. et al. Overcoming noise in entanglement distribution. *Phys. Rev. X* **9**, 041042 (2019).
22. Doda, M. et al. Quantum key distribution overcoming extreme noise: Simultaneous subspace coding using high-dimensional entanglement. *Phys. Rev. Appl.* **15**, 034003 (2021).
23. Hu, X.-M. et al. Pathways for entanglement-based quantum communication in the face of high noise. *Phys. Rev. Lett.* **127**, 110505 (2021).
24. Walborn, S., Monken, C., Pádua, S. & Souto Ribeiro, P. Spatial correlations in parametric down-conversion. *Phys. Rep.* **495**, 87–139 (2010).
25. Achatz, L. et al. Certifying position-momentum entanglement at telecommunication wavelengths. *Phys. Scr.* **97**, 015101 (2022).
26. Franson, J. D. Bell inequality for position and time. *Phys. Rev. Lett.* **62**, 2205–2208 (1989).
27. Rossi, A., Vallone, G., Chiuri, A., Martini, F. D. & Mataloni, P. Multipath entanglement of two photons. *Phys. Rev. Lett.* **102**, 153902 (2008).
28. Hu, X.-M. et al. Efficient generation of high-dimensional entanglement through multipath down-conversion. *Phys. Rev. Lett.* **125**, 090503 (2020).
29. Da Lio, B. et al. Stable transmission of high-dimensional quantum states over a 2-km multicore fiber. *IEEE J. Sel. Top. Quantum Electron.* **26**, 1–8 (2020).
30. Ortega, E. A. et al. Spatial and spectral characterization of photon pairs at telecommunication wavelengths from type-0 spontaneous parametric down-conversion. *J. Opt. Soc. Am. B* **40**, 165–171 (2023).
31. Bacco, D. et al. Characterization and stability measurement of deployed multicore fibers for quantum applications. *Photon. Res.* **9**, 1992–1997 (2021).
32. Neumann, S. P., Buchner, A., Bulla, L., Bohmann, M. & Ursin, R. Continuous entanglement distribution over a transnational 248 km fiber link. *Nat. Commun.* **13**, 2041–1723 (2022).
33. Barreiro, J. T., Wei, T.-C. & Kwiat, P. G. Beating the channel capacity limit for linear photonic superdense coding. *Nat. Phys.* **4**, 282–286 (2008).
34. Hu, X.-M. et al. Beating the channel capacity limit for superdense coding with entangled ququarts. *Sci. Adv.* **4**, eaat9304 (2018).
35. Graham, T. M., Bernstein, H. J., Wei, T.-C., Junge, M. & Kwiat, P. G. Superdense teleportation using hyperentangled photons. *Nat. Commun.* **6**, 7185 (2015).
36. Ecker, S. et al. Experimental single-copy entanglement distillation. *Phys. Rev. Lett.* **127**, 040506 (2021).
37. Wang, Q.-K. et al. High-dimensional quantum cryptography with hybrid orbital-angular-momentum states through 25 km of ring-core fiber: A proof-of-concept demonstration. *Phys. Rev. Appl.* **15**, 064034 (2021).
38. Bhalla, S. et al. Patient similarity network of newly diagnosed multiple myeloma identifies patient subgroups with distinct genetic features and clinical implications. *Sci. Adv.* **7**, eabg9551 (2021).
39. Cozzolino, D. et al. Orbital angular momentum states enabling fiber-based high-dimensional quantum communication. *Phys. Rev. Appl.* **11**, 064058 (2019).
40. Cao, H. et al. Distribution of high-dimensional orbital angular momentum entanglement over a 1 km few-mode fiber. *Optica* **7**, 232–237 (2020).
41. Wang, J., Wang, Q., Liu, J. & Lyu, D. Quantum orbital angular momentum in fibers: A review. *AVS Quantum Sci.* **4**, 031701 (2022).
42. Kim, T., Fiorentino, M. & Wong, F. N. C. Phase-stable source of polarization-entangled photons using a polarization sagnac interferometer. *Phys. Rev. A* **73**, 012316 (2006).
43. Solntsev, A. S. & Sukhorukov, A. A. Path-entangled photon sources on nonlinear chips. *Rev. Phys.* **2**, 19–31 (2017).
44. Kwiat, P. G., Steinberg, A. M. & Chiao, R. Y. High-visibility interference in a bell-inequality experiment for energy and time. *Phys. Rev. A* **47**, R2472–R2475 (1993).
45. Dietrich, P.-I. et al. Printed freeform lens arrays on multi-core fibers for highly efficient coupling in astrophotonic systems. *Opt. Express* **25**, 18288–18295 (2017).

ACKNOWLEDGEMENTS

The authors gratefully acknowledge financial support from the Austrian Academy of Sciences and the EU project OpenQKD (Grant agreement ID: 85715). E.A.O. acknowledges ANID for the financial support (Becas de doctorado en el extranjero "Becas Chile"/2016—No. 72170402). M.H. would like to acknowledge funding from the European Research Council (Consolidator grant 'Cocoquest' 101043705).

AUTHOR CONTRIBUTIONS

The energy-time setup was built by L.A. with help from L.B. and S.E. The polarization setup was built by E.A.O. The path setup was built by M.BA. with the help from L.A. The project was supervised by R.U. and M.H. The data were analyzed by L.A. and M.H. The MCF was supplied by J.C.AZ and R.AC. The paper was written by L.A. with help from S.E., M.BO. and M.H. All authors discussed the results and commented on the manuscript.

COMPETING INTERESTS

The authors declare no competing interests.

ADDITIONAL INFORMATION

Correspondence and requests for materials should be addressed to Lukas Achatz or Marcus Huber.

3.3 Certifying position-momentum entanglement at telecommunication wavelengths

In this publication we verified that our source produces position-momentum entangled photons at a wavelength of 1550nm. By scanning the x-y plane (propagation in z-axis) we measured the spatial distribution of the signal and idler photons together with their spatial correlation widths. Conducting these scans for two complementary bases, in this case position and momentum, one can violate an inferred Heisenberg uncertainty principle. The position measurement was done in the near-field while the momentum measurement was done in the far-field plane of the crystal. In order to switch from near- to far-field a different lens setup is needed, which was devised in this publication.

I contributed by planning the experiment and conducting the measurements together with Evelyn Ortega. Furthermore, I analyzed the obtained data and calculated the parameters for violating the inferred Heisenberg uncertainty principle as well as the entanglement of formation. I wrote the paper together with Martin Bohmann and with help from Evelyn Ortega.

Certifying position-momentum entanglement at telecommunication wavelengths

Physica Scripta

PAPER

Certifying position-momentum entanglement at telecommunication wavelengths

Lukas Achatz[1,2,*], **Evelyn A Ortega**[1,2], **Krishna Dovzhik**[1,2], **Rodrigo F Shiozaki**[1,3], **Jorge Fuenzalida**[1,2,4], **Sören Wengerowsky**[1,2,5], **Martin Bohmann**[1,2] and **Rupert Ursin**[1,2]

[1] Institute for Quantum Optics and Quantum Information—IQOQI Vienna, Austrian Academy of Sciences, Boltzmanngasse 3, 1090 Vienna, Austria
[2] Vienna Center for Quantum Science and Technology (VCQ), Vienna, Austria
[3] Departamento de Física, Universidade Federal de São Carlos, Rodovia Washington Luís, km 235SP-310, 13565-905 São Carlos, SP, Brazil
[4] Fraunhofer Institute for Applied Optics and Precision Engineering IOF, Albert-Einstein-Str. 7, 07745 Jena, Germany
[5] Current address: ICFO-Institut de Ciencies Fotoniques, The Barcelona Institute of Science and Technology, 08860 Castelldefels (Barcelona), Spain.
[*] Author to whom any correspondence should be addressed.

E-mail: lukas.achatz@oeaw.ac.at, martin.bohmann@oeaw.ac.at and rupert.ursin@oeaw.ac.at

Keywords: EPR Entanglement, position-momentum entanglement, SPDC source, continuous-variable entanglement

OPEN ACCESS

RECEIVED
30 June 2021

REVISED
13 December 2021

ACCEPTED FOR PUBLICATION
20 December 2021

PUBLISHED
10 January 2022

Abstract

The successful employment of high-dimensional quantum correlations and its integration in telecommunication infrastructures is vital in cutting-edge quantum technologies for increasing robustness and key generation rate. Position-momentum Einstein-Podolsky-Rosen (EPR) entanglement of photon pairs are a promising resource of such high-dimensional quantum correlations. Here, we experimentally certify EPR correlations of photon pairs generated by spontaneous parametric down-conversion (SPDC) in a nonlinear crystal with type-0 phase-matching at telecommunication wavelength for the first time. To experimentally observe EPR entanglement, we perform scanning measurements in the near- and far-field planes of the signal and idler modes. We certify EPR correlations with high statistical significance of up to 45 standard deviations. Furthermore, we determine the entanglement of formation of our source to be greater than one, indicating a dimensionality of greater than 2. Operating at telecommunication wavelengths around 1550 nm, our source is compatible with today's deployed telecommunication infrastructure, thus paving the way for integrating sources of high-dimensional entanglement into quantum-communication infrastructures.

1. Introduction

Recent scientific research in quantum information and quantum technologies focuses more and more on the exploitation of high-dimensional quantum correlations and its efficient integration into telecommunication infrastructures. In particular, high-dimensional photonic entanglement in various degrees of freedom [1–9] are an essential resource for quantum information applications. Such high-dimensional systems are particularly interesting for quantum information applications as they can be used to encode several qubits per transmitted information carrier [10–14]. Furthermore, high-dimensional entanglement features robustness against noise [15–17] that makes it an ideal candidate for realistic noisy and lossy quantum communication.

One physical realization for high-dimensional entanglement are continuous-variable position-momentum correlations of photon pairs emitted by spontaneous parametric down-conversion (SPDC) [18]. Because of energy and momentum conservation in the SPDC process, the produced continuous-variable states feature Einstein, Podolsky, and Rosen (EPR) correlations [19] that can be certified via suitable witness conditions [20–23]. Importantly, the certification of EPR-correlations directly implies entanglement. Ideally, the entangled photon pairs manifest perfect position correlations or perfect transverse momentum anti-correlations, depending on the respective basis choice, which is implemented through different lens configurations. Thus,

measurements of the two conjugate variables, position and momentum, of both photons allows to experimentally determine EPR entanglement. It is worth mentioning that this form of EPR-correlations in terms of position and momentum variables coincides with the original idea by EPR [19]. The entanglement dimensionality [24] of the signal and idler photons can, for example, be characterized by the entanglement of formation E_F [25].

The first experimental verification of EPR position-momentum entanglement of photons has been reported in [26]. Typically, sources of position-momentum entangled photons are based on type-I and type-II phase-matched SPDC sources; see, e.g., [26–30]. In these implementations, either scanning techniques [26–28, 31] or cameras [30, 32] were used to record the position and momentum observables by means of near- and far-field measurements, respectively. High E_F values and thus high-dimensional position-momentum entanglement of photons have been reported in [33]. Applications of position-momentum entangled photons are discussed in the literature, which includes ideas for quantum key distribution (QKD) [34], continuous-variable quantum computation [35], ghost-imaging applications [36] and dense-coding [37].

Despite its huge potential as mentioned above, high-dimensional position-momentum EPR-entanglement from SPDC sources are underrepresented among the quantum information applications. This has practical reasons. Firstly, the direct detection of photons using cameras makes further manipulations of the photons impossible and thus hinders the application of quantum information protocols. Secondly, the wavelength of the photons used in the majority of position-momentum experiments is not compatible with the current telecommunication infrastructure which works best between 1260 nm and 1625 nm, where optical loss is lowest [38]. Additionally, most experiments use type-II phase-matched SPDC-crystals to produce the entangled photon pairs, which have a relatively low brightness and narrow spectrum as compared to type-0 phase-matched SPDC-crystals [39].

In this paper, we report on a bright source producing position-momentum EPR-entangled photons at telecommunication wavelengths allowing for the efficient integration into existing quantum communication infrastructures. We generate photons via SPDC in a Magnesium Oxide doped periodically poled Lithium Niobate (MgO:ppLN) crystal with type-0 phase-matching in a Sagnac-configuration with a center-wavelength of 1550.15 nm. We evaluate near- and far-field correlations by probabilistically splitting the photon-pairs at a beamsplitter and transversely scanning two fibers in (x_1, y_1) and (x_2, y_2) directions respectively. The photons in each fiber were counted with a superconducting nanowire single-photon detector (SNSPD) and a time tagging device connected to a readout-system. The temporal correlation between the time tags was later analyzed. Based on these measurements, we certify position-momentum EPR-entanglement with high statistical significance. We further calculate the entanglement of formation of the photon pairs to be greater than 1, indicating a dimensionality of greater than 2. Furthermore, our setup is stable over several hours and the used imaging system is capable of coupling the entangled photons into photonic waveguides. In addition, our source can be extended to hyper-entanglement experiments harnessing entanglement in the position-momentum as well as polarization degree of freedom. To the best of our knowledge, this is the first demonstration of position-momentum EPR-entangled photon pairs from a type-0 phase-matched SPDC source at telecommunication wavelength. Our results show the possibility of utilizing the high-dimensional characteristic of continuous-variable EPR-entanglement for this regime and, thus, enable its integration in existing telecommunication quantum-communication systems.

2. Experiment

In our experiment, we studied and characterized the position-momentum entanglement of photon pairs. For this purpose, we generated photon pairs at telecommunication wavelength from a type-0 phase-matched SPDC-source in a Sagnac configuration [40]. By measuring the distributions of the signal and idler photons in the near- and far-field we obtained their position and momentum correlations. With these we can investigate EPR-correlations in position and moment of the photon pairs. It is worth mentioning that certifying EPR-correlations directly implies entanglement between signal and idler photons. In this sense, demonstrating EPR-correlations is a stronger and more direct indication of the non-local character of quantum mechanics [22] which, however, is in general more demanding than verifying entanglement.

The experimental setup is shown in figure 1. The heart of the SPDC-source is a 40-mm-long ppLN bulk crystal with a poling period of 19.2 μm. The crystal was pumped with a continuous-wave (CW) laser at 775.078 nm, 10 mW pump power and a pump-beam waist (FWHM) at the center of the crystal of 83.5 μm. In the parametric process, one pump photon is converted with low probability to a pair of signal and idler photons in the telecommunication wavelength regime of around 1550 nm. The emission angles of the emitted photons during the SPDC process strongly depend on the temperature of the crystal. By controlling the temperature of the crystal we adjust a non-collinear, quasi-phase-matched SPDC process. Due to the

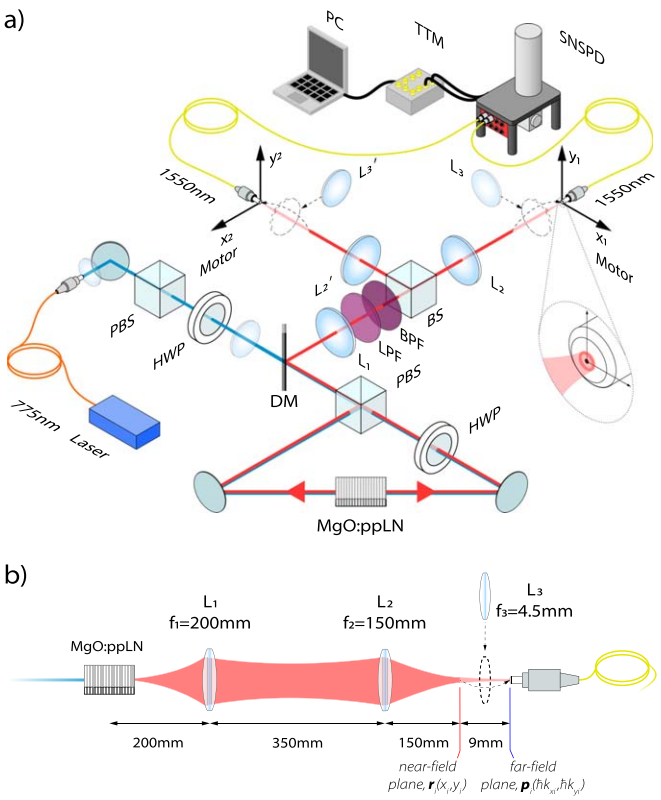

Figure 1. (a) Setup used to measure the coincidences in near- and far-field. The laser emits light at a center wavelength of 775.078 nm. The beam is slightly focused into a 40-mm-long ppLN type-0 phase-matched crystal. After the crystal two lens configurations are used to implement the near- and far-field measurements. The focal lengths of the lenses are $f_1 = 250$ mm, $f_2 = f_2' = 200$ mm and $f_3 = f_3' = 4.5$ mm. (b) Simplified setup showing the lens configurations. In analogy with the polarization basis, different lens configurations correspond to different complementary basis choices. For the near-field measurement (position-space, photon pairs show correlation), L_3 (L_3') was not mounted in the setup and the fiber was placed in the focal point of lens L_2 (L_2'). For the far-field measurement (momentum-space, photon pairs show anti-correlation), L_3 (L_3') was mounted at the focal distance $f_2 + f_3$ ($f_2' + f_3'$) and the fiber was moved back for 9 mm, thus aligning it with the focal distance of L_3 (L_3').

momentum conservation in the SPDC process, the signal and idler photons are emitted with opposite transverse (x-y-plane) momentum-vectors, meaning that $\mathbf{p}_1 = -\mathbf{p}_2$ with $\mathbf{p}_i = (\hbar k_{x_i}, \hbar k_{y_i})$, where k refers to the transverse wave-vector and $i = 1, 2$. Thus, when imaging the photons in the far-field plane of the crystal, one can observe anti-correlations in the coincidence counts. From hereon indices 1 and 2 refer to signal and idler photon, respectively. Since the photons of each pair are created at the same point in space, imaging the photons in the near-field results in correlations, meaning that $r_1 = r_2$, with $\mathbf{r}_i = (x_i, y_i)$ and $i = 1, 2$.

Note that through the Sagnac configuration the nonlinear crystal is bidirectionally pumped. In this way, the produced photon pairs not only exhibit position-momentum entanglement but are also entangled in polarization [40], although this degree of freedom was not investigated in this work.

After the Sagnac loop, the SPDC photons were separated from the pump beam with a dichroic mirror (DM) and spectrally cleaned with a long-pass filter (LPF, $\lambda_{\mathrm{cut-off}} = 780$ nm) and a band-pass filter (BPF, $\lambda_{\mathrm{BPF}} = 1550 \pm 3$ nm). After the first lens (L_1), a beam splitter (BS) separates signal and idler photons probabilistically for 50% of the incoming pairs. To perform the near-field (position) and far-field (momentum) measurements of the photon pairs, two different lens configurations are used; cf also figure 1(b). The far-field measurement of the signal and idler photons is implemented via L_1 with a focal length of $f_1 = 200$ mm. L_1 acts as a Fourier lens that maps the transverse position of the photons to transverse momentum in the far-field plane. Then, the far-field plane is imaged and demagnified by two consecutive lenses L_2 (L_2') and L_3 (L_3') with focal lengths of $f_2 = f_2' = 150$ mm and $f_3 = f_3' = 4.5$ mm, resulting in a demagnification factor of $M_{\mathrm{FF}} = f_3/f_2 = f_3'/f_2' = 0.03$. This results in an effective focal length of the Fourier lens of 6 mm. For the near-field measurement, the crystal plane is imaged with a $2f/2f'$ optical system by L_1 and L_2 (L_2'). This configuration results in a magnification factor of $M_{\mathrm{NF}} = f_2/f_1 = f_2'/f_1 = 0.75$. Note that the used imaging system would allow for the integration of the near and far-field measurements in (micro-)photonic architectures, such as multicore fibers [41] or photonic chips [42].

In two consecutive measurement runs, we measured the coincidences of the correlated photons in the near- and far-field. A coincidence count was identified when both detector-channels register photons within a 300 ps

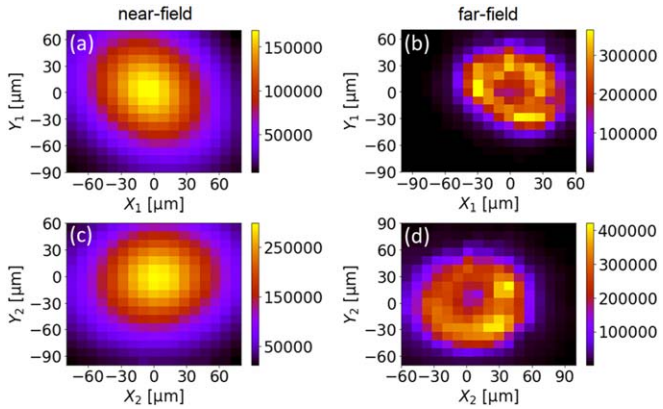

Figure 2. Measured average single counts per second for every (x_i, y_i) in the near-field (a), (c) and the far-field (b), (d) for the signal $(i = 1)$ and idler $(i = 2)$ modes. To obtain the average single counts per second for every (x_1, y_1) position, we averaged the recorded counts of the signal mode over all positions of the (x_2, y_2) detection stage, which corresponds to an integration time of 17^2 s. The same procedure is performed to determine the average single counts of the idler beam along (x_2, y_2).

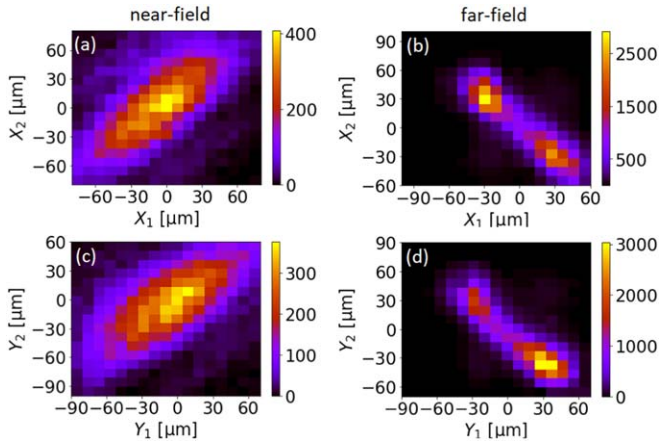

Figure 3. Measured coincident counts for every (x_1, x_2) and (y_1, y_2) in the near-field (a), (c) and the far-field (b), (d). For plotting the (x_1, x_2) case, the (y_1, y_2) fiber positions were taken to be at 0 μm. For the (y_1, y_2) case, the (x_1, x_2) fiber positions were taken to be at 0 μm.

time-window. These measurements were achieved by performing a transverse plane-scan with two single-mode fibers (SMF), which guide the photons to a SNSPD and read-out electronics. Such scanning approaches have already been used to characterize the spatial correlations for type-II SPDC-sources [26–28]. Arrival times were tagged using a time-tagging-module (TTM), combining the photon counts with the positions of the translation stages at all times. The scans were performed for both settings (near- and far-field) in the signal and idler arms Using motorized translation stages, each coordinate was sampled in 17 steps with a step size of 10 μm, which results in a 17×17 grid on each detection side and a total of $17^4 = 83.521$ data points. For each data point we measured 1 s and recorded the single counts of each detector and the coincidence-counts between both detectors. The total measurement time was about 80 h, throughout which the whole setup was stable.

3. Results

3.1. Scan results

The results for the near- and far-field scans are summarized in figures 2 and 3. For both measurement settings (either near- or far-field), we obtained the single counts at the motor-positions (x_1, y_1) and (x_2, y_2) as well as the coincidence counts between both detection stages at (x_1, y_1, x_2, y_2). The maximum single-photon count-rate in the near-field (far-field) was about 150 kHz (300 kHz) for signal and about 250 kHz (400 kHz) for the idler mode. The maximum coincident-photon count-rate in the near-field (far-field) was about 500 Hz (3000 Hz) for both signal and idler modes. The discrepancy between the count rates of signal and idler modes can be explained by different coupling efficiencies into the single-mode fibers. To obtain the average single counts for every (x_1, y_1) position, we averaged the recorded counts of the signal mode over all positions of the (x_2, y_2)

detection stage, which corresponds to an integration time of 17^2 s. The same procedure is performed to determine the average single counts of the idler beam along (x_2, y_2). Figure 2 displays the averaged single counts in the signal and idler modes. In figure 3 the correlation between every (x_1, x_2) and (y_1, y_2) coordinate pair is shown.

In both figures, the expected features of the non-collinear SPDC emission in the near- and far-field are reflected: in the near-field, the photon pairs follow a Gaussian distribution. For the single counts the shape is basically given by the intensity distribution (beam waist) of the pump beam in the center of the nonlinear crystal, while for the coincident counts the Gaussian form is given by the form of the joint wave function in **r**-space [43]. And in far-field the anti-correlations in the transverse momenta, stemming from the non-collinear quasi-phase-matched SPDC process, manifests itself in a doughnut or ring-shape structure. We note that no data-correction or post-processing, such as subtraction of dark counts, was performed. In particular, no accidental coincidences were subtracted as is required in experiments using cameras [30, 32]. The visible asymmetries can be explained by imperfect optical components and changing focusing parameters during the scans.

When comparing the single counts of signal and idler modes, a discrepancy of about 30% is visible. This can be explained by the different coupling efficiencies of the used fibers. The slight difference in the count rates does, however, not influence the quality of the measured entanglement, as it is analyzed based on coincidence detection.

Furthermore, from figures 2(a) and (c) and taking into account the magnification of the lens-setup we estimate the diameter of the photon-pair birth region inside the crystal to be $\approx$80 μm. This is in very good agreement with the pump-beam waist of 83.5 μm at the crystal and thus provides a suitable sanity check of the results.

Based on the recorded scans in the near- and far-field of the signal and idler photons, we now analyze the position and momentum quantum correlations of our telecom-wavelength type-0 phase-matched SPDC-source. Firstly, we will verify the EPR-type entanglement based on the spatial spread between the coincidence counts of signal and idler photons. Secondly, we estimate the entanglement dimensionality by determining E_F in both scan directions.

3.2. Certifying EPR entanglement

Position-momentum entanglement of the signal and idler modes can be certified by violating a so-called EPR-Reid criterion. For this we are introducing the following local-realistic premises [19, 22]:

Realism: If, without in any way disturbing a system, we can predict with some specified uncertainty the value of a physical quantity, then there exists a stochastic element of physical reality which determines this physical quantity with at most that specific uncertainty.

Locality: A measurement performed at a spatially separated location 1 cannot change the outcome of a measurement performed at a location 2.

In the following argument the receiver of the signal photon is referred to as Alice, while the receiver of the idler photon is referred to as Bob. The argumentation goes as follows: When Bob measures the position x_2 of particle 2 he can then estimate, with some uncertainty, the position x_1 of particle 1 at Alice's site. The average inference variance of this estimate $x_1^{\mathrm{est}}(x_2)$ is defined as follows [22, 23]:

$$\Delta^2_{\mathrm{inf}}(x_1|x_2) \equiv \int dx_1 P(x_1|x_2)[x_1 - x_1^{est}(x_2)]^2 \tag{1}$$

where $P(x_1|x_2)$ is the conditional probability to measure x_1 if x_2 has already been measured. The minimum of this inferred variance is obtained when the estimated value $x_1^{\mathrm{est}}(x_2)$ is the expectation value of x_1. Thus, the minimum inferred variance for a position measurement is given by

$$\Delta^2_{\mathrm{min}}(\mathbf{r}_1|\mathbf{r}_2) = \int d\mathbf{r}_2 P(\mathbf{r}_2)\Delta^2(\mathbf{r}_1|\mathbf{r}_2) \tag{2}$$

and

$$\Delta^2_{\mathrm{min}}(\mathbf{p}_1|\mathbf{p}_2) = \int d\mathbf{p}_2 P(\mathbf{p}_2)\Delta^2(\mathbf{p}_1|\mathbf{p}_2) \tag{3}$$

for a momentum measurement. Here $\Delta^2(\mathbf{r}_1|\mathbf{r}_2)$ is the uncertainty (i.e. variance) in $\mathbf{r}_1$ for a fixed $\mathbf{r}_2$ and $P(\mathbf{r}_2)$ represents the probability distribution of $\mathbf{r}_2$ which are experimentally determined via the relative count frequencies. The minimum inferred variance for the transverse momenta $\Delta^2_{\mathrm{min}}(\mathbf{p}_1|\mathbf{p}_2)$ is defined analogously. The argument continues as follows: Since Bob is able to infer the outcome of either a position or momentum measurement at Alice's site within some uncertainty and since the locality assumption does not allow a measurement to induce change at a spatially separated location, in a local-realistic picture it follows that statistical elements of reality determining the position and momentum of both particles must exist at the same time. The precision with which one can measure the position and momentum of a particle is fundamentally limited by Heisenberg's uncertainty principle $\Delta x \Delta p \geqslant \frac{\hbar}{2}$. By measuring the position and momentum of

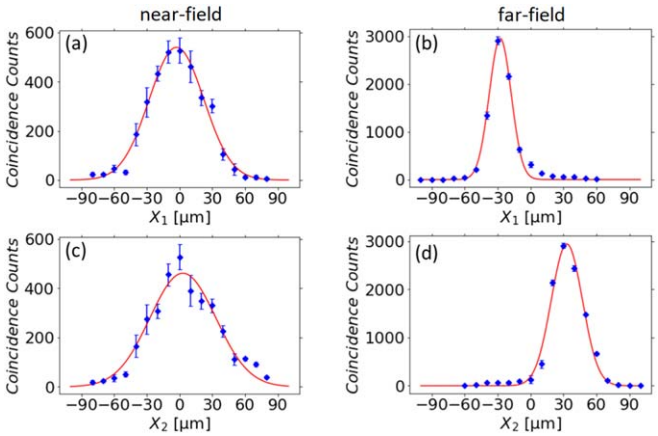

Figure 4. Example cases for the Gauss-fits of the obtained coincidence counts for the x coordinate. For calculating the minimum inferred variance for the entire x_1-axis according to equation (3), the fiber positions of x_2 were ranging from -40 μm to $+40$ μm with a stepsize of 10 μm. At every step the data was fitted and the standard deviation calculated. The values on the abscissa represent the position of the fibers. The minimum inferred variances were then obtained by integration over the respective coordinate, according to equation (3). (a) Coincidence counts in the near-field for $(x_1, y_1, x_2, y_2) = (x_1, 0, 0, 0)$. (b) Coincidence counts in the far-field for $(x_1, y_1, x_2, y_2) = (x_1, 0, +30\ \mu\text{m}, 0)$. (c) Coincidence counts in the near-field for $(x_1, y_1, x_2, y_2) = (0, 0, x_2, 0)$. (d) Coincidence counts in the far-field for $(x_1, y_1, x_2, y_2) = (-30\ \mu\text{m}, 0, x_2, 0)$.

particles with higher accuracy than permitted by Heisenberg's uncertainty principle, the local-realistic assumptions cannot hold. Thus, EPR-correlations can be certified by violating following inequality [21–23]:

$$\Delta^2_{\text{min}}(\mathbf{r}_1|\mathbf{r}_2)\,\Delta^2_{\text{min}}(\mathbf{p}_1|\mathbf{p}_2) > \frac{\hbar^2}{4}. \tag{4}$$

Here, $\Delta^2_{\text{min}}(\mathbf{r}_1|\mathbf{r}_2)$ is the minimum inferred variance, which represents the minimum uncertainty in inferring transverse position $\mathbf{r}_1$ of the signal mode conditioned upon measuring $\mathbf{r}_2$ in the idler mode.

For the calculation of the minimum inferred variances in the x-direction, we only took into account the values on the abscissa, meaning that $y_1 = y_2 = 0$. As for the y-direction, only values along the ordinate axis, where $x_1 = x_2 = 0$, were taken into account. We also treated the x and y components separately as they correspond to commuting observables.

In accordance with previous experiments [26–30], we determined the minimal inferred variances in near and far-field by fitting the conditional uncertainties $\Delta^2(\mathbf{r}_1|\mathbf{r}_2)$ and $\Delta^2(\mathbf{p}_1|\mathbf{p}_2)$ with Gaussian functions of the form (here formulated for x_1 with a fixed position x_2):

$$\Psi(x_1|x_2) = \mathcal{N}\exp\left[\frac{-(x_1-\mu)^2}{4\sigma^2_{x_1}}\right] \tag{5}$$

where $\mathcal{N}$ is a normalization constant, μ is the expectation value and σ_{x_1} is the standard deviation, i.e. the uncertainty along the x_1 direction. For an extensive discussion of this approach the reader is referred to [44]. Exemplarily, we show for four cases the data and the corresponding Gaussian fits in figure 4. From the obtained standard deviations one can then calculate the conditional near-field variances by taking into account the magnification of our imaging system

$$\Delta^2(x_1|x_2) = \left(\frac{\sigma_{x_1}}{M_{\text{NF}}}\right)^2. \tag{6}$$

The same procedure is repeated for y_1, x_2 and y_2.

For the far-field measurement the procedure is analogous. To translate the obtained standard deviations to the actual conditional momentum variances following relation is used [45]:

$$\Delta^2(p_{x_1}|p_{x_2}) = \left(\frac{2\pi\hbar}{\lambda f_1 M_{\text{FF}}}\sigma_{x_1}\right)^2, \tag{7}$$

where λ is the wavelength of the entangled photons, f_1 is the focal length of the Fourier lens L_1 and σ_{x_1} is the standard deviation as obtained by the Gauss-fit. The same procedure is repeated for p_{y_1}, p_{x_2} and p_{y_2}. The obtained values for the minimum inferred variances calculated with equation (3) are listed in table 1.

Based on the minimal inferred variances we can now test for EPR correlations via equation (4). The values of the left-hand-side of equation (4) for the different cases are listed in table 1. In all cases, we observe a clear violation of the inequality which certifies EPR-correlations between the signal and idler photons in their

Table 1. Obtained minimum variances from fitting a Gaussian-function in the form of equation (5) to the obtained raw-data. The obtained values are calculated according to equation (6) for $\Delta^2_{\min}(x_i|x_j)$ and equation (7) for $\Delta^2_{\min}(q_{x_i}|q_{x_j})$. The uncertainty product is then calculated by multiplying the minimum inferred variances. A clear violation of inequality (4) is shown. The errors of the obtained values stem both form the Poisson distribution of the photons as well as the Gaussian fit, while the errors of the uncertainty product were calculated with standard Gaussian error propagation.

Minimum variance	Obtained values	Uncertainty product
$\Delta^2_{\min}(x_1\|x_2)$	$(6.6 \pm 0.6) \times 10^{-4}\,\mathrm{mm}^2$	$[(2.4 \pm 0.5) \times 10^{-2}\hbar^2]$
$\Delta^2_{\min}(p_{x_1}\|p_{x_2})$	$(37.1 \pm 6.1)\hbar^2\mathrm{mm}^{-2}$	
$\Delta^2_{\min}(y_1\|y_2)$	$(9.2 \pm 0.7) \times 10^{-4}\,\mathrm{mm}^2$	$[(3.7 \pm 0.6) \times 10^{-2}\hbar^2]$
$\Delta^2_{\min}(p_{y_1}\|p_{y_2})$	$(39.8 \pm 6.3)\hbar^2\mathrm{mm}^{-2}$	
$\Delta^2_{\min}(x_2\|x_1)$	$(7.8 \pm 0.9) \times 10^{-4}\,\mathrm{mm}^2$	$[(3.7 \pm 0.7) \times 10^{-2}\hbar^2]$
$\Delta^2_{\min}(p_{x_2}\|p_{x_1})$	$(46.8 \pm 6.8)\hbar^2\mathrm{mm}^{-2}$	
$\Delta^2_{\min}(y_2\|y_1)$	$(7.0 \pm 0.5) \times 10^{-4}\,\mathrm{mm}^2$	$[(3.4 \pm 0.5) \times 10^{-2}\hbar^2]$
$\Delta^2_{\min}(p_{y_2}\|p_{y_1})$	$(48.1 \pm 6.9)\hbar^2\mathrm{mm}^{-2}$	

Table 2. Obtained values for the entanglement of formation (E_F) based on the conditional standard deviations along the x- and y-axes scans in the near- and far-field. The standard deviations are obtained by fitting Gaussian functions in the form of equation (5) to the data and using equations (6) and (7).

Standard deviation	Obtained values	E_F
$\Delta(x_1\|x_2)$	$(3.12 \pm 0.15)\times 10^{-2}\,\mathrm{mm}$	$[(1.30 \pm 0.10)]$
$\Delta(k_{x_1}\|k_{x_2})$	$(4.79 \pm 0.24)\,\mathrm{mm}^{-1}$	
$\Delta(y_1\|y_2)$	$(3.18 \pm 0.19)\times 10^{-2}\,\mathrm{mm}$	$[(1.18 \pm 0.13)]$
$\Delta(k_{y_1}\|k_{y_2})$	$(5.09 \pm 0.35)\,\mathrm{mm}^{-1}$	

position-momentum degree of freedom. In particular, inequality (4) is violated by up to 45 standard deviations, which demonstrates the high statistical significance of our results as well as the degree to which our system deviates from a local-realistic one. Thus, we could certify position-momentum entanglement from a type-0 phase-matched SPDC-source at telecommunication wavelength.

3.3. Entanglement of formation and entanglement dimensionality

A key advantage of continuous-variable entanglement lies in the fact that, in principle, the underlying infinite-dimensional Hilbert can be exploited [46]. This means that high-dimensional quantum information protocols can be employed which go beyond the entanglement structure of qubit systems as, for example, in the case of polarization entangled photon pairs. To certify high-dimensional entanglement in our experiment, we use the entanglement of formation E_F that is defined as the number of Bell states necessary to fully describe the system [25]. Importantly, E_F provides a lower bound to the entanglement dimensionality D through $D \geqslant 2^{E_\mathrm{F}}$. In particular, this means that $E_\mathrm{F} > 1$ implies an entanglement dimensionality of at least 3. Hence, the entanglement of formation serves as a way of certifying and quantifying high-dimensional entanglement.

To characterize the dimensionality of the position-momentum entanglement attainable from our source, we estimate the E_F of the entangled photon pairs along the x-axis via [47]:

$$E_\mathrm{F} \geqslant -\log_2(\mathrm{e}\ \Delta(x_1|x_2)\ \Delta(k_{x_1}|k_{x_2})), \tag{8}$$

where $\Delta(x_1|x_2)$ and $\Delta(k_{x_1}|k_{x_2})$ are the measured standard deviations as obtained by the Gauss-fit from equation (5) and transformed with equations (6) and (7), respectively. For this purpose, we consider the scans where the count rates are highest, which is along $(x_1, y_1, x_2, y_2) = (x_1, 0, 0, 0)$ in the near-field plane and $(x_1, y_1, x_2, y_2) = (x_1, 0, +30\ \mu\mathrm{m}, 0)$ in the far-field plane, stemming from the non-collinear SPDC process. The entanglement of formation along the y-axis is defined similarly, and we determine it based on the near- and far-field plane scans along $(x_1, y_1, x_2, y_2) = (0, y_1, 0, 0)$ and $(x_1, y_1, x_2, y_2) = (0, y_1, 0, +30\ \mu\mathrm{m})$, respectively. The calculated values for the x and y scans and the resulting values of E_F are listed in table 2. For both directions E_F is greater than 1, implying an entanglement dimensionality of at least 3 in either direction.

At this point it has to be stressed that the entanglement dimensionality strongly depends on the length of the SPDC crystal. A shorter crystal results in a higher degree of position-momentum entanglement [44]. In other

experiments [26, 28, 30, 33] the crystal length does not exceed 5 mm, as compared to the 40 mm-long crystal used in this experiment, which explains the relatively low values of the calculated entanglement of formation and entanglement dimensionality and also suggests that, in principle, a much higher entanglement dimensionality could be achieved with our setup by adapting the crystal length.

4. Conclusion

Our experiment exhibits several important features which need to be highlighted.

Firstly, it is important to stress that the entangled photon pairs are created at wavelengths around 1550 nm, thus at the C-Band of the telecommunication infrastructure. Operating sources in this wavelength regime allows for the integration into modern and future telecommunication infrastructures and increases the transmission rate over long distances.

Secondly, with the possibility to distribute position-momentum-entangled photons efficiently, it is possible to exploit the entanglement for quantum communication purposes. This allows to implement quantum key distribution based on the photons' EPR correlations [34]: by randomly choosing different measurement settings (near- and far-field) and distributing the photons to the two communication partners via two fibers a secret key can be shared. Recent developments in quantum communication using multicore fibers [41] also suggest that position-momentum-entangled photon pairs can be distributed through several cores simultaneously. Thus, multicore fibers provide a pathway to high-dimensional encoding and multiplexed distribution [48]. In this context it is important to mention that the used imaging system facilitates the coupling of the entangled photon pairs into multicore fibers or other mircophotonic architectures, which allows for a direct coupling into such platforms.

Thirdly, the presented experimental setup features the possibility to exploit quantum hyper-correlations, i.e., simultaneous entanglement in different degrees of freedom. The Sagnac configuration of our source produces not only position-momentum entanglement but also entanglement between the polarization degrees of freedom of the photon pairs. Although we did not characterize the polarization entanglement in this experiment, it is possible to utilize this additional degree of freedom in hybrid quantum information tasks. Such a hybrid strategy can offer a significant increase of the overall dimensionality as it scales with the product of the dimensionalities of the individual degrees of freedom. Finally, it is important to highlight the long-term stability of the experimental setup over a period of several days that renders the implementation of stable quantum information applications possible.

The obtained standard deviations are in good agreement with values reported in previous experiments, as for example in [26, 32], although about 2 orders of magnitude lower than the value reported in [30]. When comparing the entanglement of formation with the latest publications, for example [30, 33], it is apparent that the dimensionalities obtained here are far lower. The reason for this is the comparably long crystal and the focused pump beam. By adjusting and optimizing these parameters, the entanglement and hence the dimensionality can be increased.

We have performed a position-momentum correlation measurement of photon pairs at telecommunication wavelength generated in a non-collinear, type-0 phase-matched SPDC process. For this purpose, we measured the position and momentum correlations of the generated signal and idler photons by recording the near- and far-field correlations, respectively, using a scanning technique. Based on the obtained correlation data, we certified EPR correlations, and consequently entanglement, of the signal-idler pairs with high statistical significance of 45 standard deviations. We characterized the underlying high-dimensional entanglement further by estimating the entanglement of formation from our source. The calculated E_F value greater than one implies an entanglement dimensionality of at least three in both scan directions. Note that the dimensionality can easily be increased by using a shorter crystal or a less focused pump-beam. To the best of our knowledge, this is the first experimental certification and characterization of position-momentum correlations from a type-0 phase-matched SPDC source at telecommunication wavelength.

In a nutshell, we produced and certified position-momentum entanglement of photon pairs in the telecommunication wavelength regime which allows for the integration to telecommunication infrastructures and can be further extended to quantum hyper-correlations using several degrees of freedom in parallel.

Acknowledgments

We gratefully acknowledge financial support from the Austrian Academy of Sciences and the EU project OpenQKD (Grant agreement ID: 85 715). E A O and J F acknowledge ANID for the financial support (Becas de doctorado en el extranjero 'Becas Chile'/2016—No. 72 170 402 and 2015—No. 72 160 487). L A also thanks James Schneeloch and Marcus Huber for insightful comments.

Data availability statement

The data that support the findings of this study are available upon reasonable request from the authors.

ORCID iDs

Martin Bohmann https://orcid.org/0000-0003-3857-4555

References

[1] Mirhosseini M, Magaña-Loaiza O S, O'Sullivan M N, Rodenburg B, Malik M, Lavery M P J, Padgett M J, Gauthier D J and Boyd R W 2015 *New J. Phys.* **17** 033033
[2] Gerke S, Sperling J, Vogel W, Cai Y, Roslund J, Treps N and Fabre C 2015 *Phys. Rev. Lett.* **114** 050501
[3] Steinlechner F, Ecker S, Fink M, Liu B, Bavaresco J, Huber M, Scheidl T and Ursin R 2017 *Nat. Commun.* **8** 15971
[4] Wang J *et al* 2018 *Science* **360** 285–91
[5] Ansari V, Donohue J M, Brecht B and Silberhorn C 2018 *Optica* **5** 534–50
[6] Kysela J, Erhard M, Hochrainer A, Krenn M and Zeilinger A 2020 *Proc. Natl Acad. Sci.* **117** 26118–22
[7] Hu X M, Xing W B, Liu B H, Huang Y F, Li C F, Guo G C, Erker P and Huber M 2020 *Phys. Rev. Lett.* **125** 090503
[8] Chen Y, Ecker S, Bavaresco J, Scheidl T, Chen L, Steinlechner F, Huber M and Ursin R 2020 *Phys. Rev.* A **101** 032302
[9] Erhard M, Krenn M and Zeilinger A 2020 *Nature Reviews Physics* **2** 365–81
[10] Bechmann-Pasquinucci H and Tittel W 2000 *Phys. Rev.* A **61** 062308
[11] Aolita L and Walborn S P 2007 *Phys. Rev. Lett.* **98** 100501
[12] Ali-Khan I, Broadbent C J and Howell J C 2007 *Phys. Rev. Lett.* **98** 060503
[13] Mower J, Zhang Z, Desjardins P, Lee C, Shapiro J H and Englund D 2013 *Phys. Rev.* A **87** 062322
[14] Graham T M, Bernstein H J, Wei T C, Junge M and Kwiat P G 2015 *Nat. Commun.* **6** 7185
[15] Ecker S *et al* 2019 *Phys. Rev.* X **9** 041042
[16] Doda M, Huber M, Murta G, Pivoluska M, Plesch M and Vlachou C 2020 *Phys. Rev. Applied* **15** 034003
[17] Hu X M *et al* 2021 *Phys. Rev. Lett.* **127** 110505
[18] Walborn S, Monken C, Pádua S and Souto Ribeiro P 2010 *Phys. Rep.* **495** 87–139
[19] Einstein A, Podolsky B and Rosen N 1935 *Phys. Rev.* **47** 777–80
[20] Reid M D and Drummond P D 1988 *Phys. Rev. Lett.* **60** 2731–3
[21] Reid M D 1989 *Phys. Rev.* A **40** 913–23
[22] Reid M D, Drummond P D, Bowen W P, Cavalcanti E G, Lam P K, Bachor H A, Andersen U L and Leuchs G 2009 *Rev. Mod. Phys.* **81** 1727–51
[23] Cavalcanti E G, Jones S J, Wiseman H M and Reid M D 2009 *Phys. Rev.* A **80** 032112
[24] Terhal B M and Horodecki P 2000 *Phys. Rev.* A **61** 040301
[25] Bennett C H, DiVincenzo D P, Smolin J A and Wootters W K 1996 *Phys. Rev.* A **54** 3824–51
[26] Howell J C, Bennink R S, Bentley S J and Boyd R W 2004 *Phys. Rev. Lett.* **92** 210403
[27] O'Sullivan-Hale M N, Ali Khan I, Boyd R W and Howell J C 2005 *Phys. Rev. Lett.* **94** 220501
[28] Ostermeyer M, Korn D, Puhlmann D, Henkel C and Eisert J 2009 *J. Mod. Opt.* **56** 1829–37
[29] Moreau P A, Devaux F and Lantz E 2014 *Phys. Rev. Lett.* **113** 160401
[30] Edgar M, Tasca D, Izdebski F, Warburton R, Leach J, Agnew M, Buller G, Boyd R and Padgett M 2012 *Nat. Commun.* **3** 984
[31] Schneeloch J, Knarr S H, Lum D J and Howell J C 2016 *Phys. Rev.* A **93** 012105
[32] Eckmann B, Bessire B, Unternährer M, Gasparini L, Perenzoni M and Stefanov A 2020 *Opt. Express* **28** 31553–71
[33] Schneeloch J, Tison C C, Fanto M L, Alsing P M and Howland G A 2019 *Nat. Commun.* **10** 2785
[34] Almeida M P, Walborn S P and Souto Ribeiro P H 2005 *Phys. Rev.* A **72** 022313
[35] Tasca D S, Gomes R M, Toscano F, Souto Ribeiro P H and Walborn S P 2011 *Phys. Rev.* A **83** 052325
[36] Pittman T B, Shih Y H, Strekalov D V and Sergienko A V 1995 *Phys. Rev.* A **52** R3429–32
[37] Bennett C H and Wiesner S J 1992 *Phys. Rev. Lett.* **69** 2881–4
[38] Ghatak A K and Thyagarajan K 2008 *Fundamentals of Photonics* **1** 262–3
[39] Steinlechner F, Gilaberte M, Jofre M, Scheidl T, Torres J P, Pruneri V and Ursin R 2014 *J. Opt. Soc. Am.* B **31** 2068–76
[40] Kim T, Fiorentino M and Wong F N C 2006 *Phys. Rev.* A **73** 012316
[41] Xavier G B and Lima G 2020 *Communications Physics* **3** 9
[42] Wang J, Sciarrino F, Laing A and Thompson M G 2020 *Nat. Photonics* **14** 273–84
[43] Monken C H, Ribeiro P H S and Pádua S 1998 *Phys. Rev.* A **57** 3123–6
[44] Schneeloch J and Howell J C 2016 *J. Opt.* **18** 053501
[45] Saleh B E A and Teich M C 1991 *Wiley* **1** 108–56
[46] Horodecki R, Horodecki P, Horodecki M and Horodecki K 2009 *Rev. Mod. Phys.* **81** 865–942
[47] Schneeloch J and Howland G A 2018 *Phys. Rev.* A **97** 042338
[48] Ortega E, Dovzhik K, Fuenzalida J, Soeren Wengerowsky J C A Z, Shiozaki R F, Amezcua-Correa R, Bohmann M and Ursin R 2021 *PRX Quantum* **2** 040356

CHAPTER 4
CONCLUSION

The publications which were written during the course of this thesis are investigating the process of building and characterizing an entangled photon-source, how to reliably transmit entanglement in multiple degrees of freedom through a multi-core fiber and eventually detecting and certifying entanglement with various methods.

Starting with **Publication** 3.1, a thorough characterization of the utilized photon-source is a necessary condition for future experiments. Here, we were measuring the incoherence of one subsystem to quantify the degree of entanglement within the entire system through the inverse purity ("Schmidt Number"). This measure allows the experimenter to conveniently quantify the apparent entanglement via intensity measurements on one subsystem. Since the opening angle of the emission cone as well as the quality of entanglement are strongly dependent on the crystal temperature, the measurements conducted in **Publication** 3.1 mark an important contribution for finding an optimal balance between those parameters. By combining these results with experiments utilizing multi-core fibers [48] and the technique of creating quantum communication networks via multiplexing [6], entirely new implementations are enabled, solely controlled by the easily tunable crystal temperature. One could, for instance, implement network-communication scenarios with multi-core fibers where the routing of photon-pairs is controlled over the crystal temperature.

In **Publication** 3.2 we directly utilized this knowledge of the dependency between crystal temperature and emission cone to optimize the coincidence count rates for cou-

pling into a multi-core fiber. We furthermore reported the first simultaneous transmission of hyper-entanglement in the degree of polarization, energy-time and path through this multi-core fiber. We achieved visibilities as high as 95% in every DOF, far beyond the limit of 81% needed for quantum key distribution protocols. By utilizing multi-core fiber technology combined with multiple (continuous) DOFs the noise resilience [45, 46, 47] as well as the obtainable secure key rate [58, 59, 60] is greatly improved. Another advantage of using multiple DOFs simultaneously is that loss of entanglement through decoherence in one DOF does consequently not hinder secure key creation in another DOF. It is important to note that by using a micro-lens array [61] in front of the MCF facet one can greatly increase the heralding efficiency, i.e. the ratio of coincidences to singles, of our source. By optimizing the heralding efficiency the secure key rate is directly increased as well. The used wavelength of 1560 nm lies in the C-band (1530 nm to 1565 nm [62]) of state-of-the-art fiber telecommunication. This makes our approach compatible with deployed fiber infrastructure, thus paving the way for future high-capacity quantum communication networks.

In **Publication** 3.3 we investigate the continuous position-momentum DOF in the way it was first proposed by Einstein, Podolsky and Rosen [16] in 1935. Here, the entanglement witness as constructed in [55] is used for certification and we were able to prove entanglement by over 45 standard deviations. The scanning procedure applied within this publication is a useful tool to investigate the spatial spread of the entangled photons. The applications for position-momentum entangled photons include quantum key distribution (QKD) [63], continuous-variable quantum computation [64], ghost-imaging applications [65] and dense-coding [66]. The wavelength of 1550 lies again in the C-band, thus creating a pathway for incorporating those application ideas into real-world scenarios.

To summarize, the publications within this thesis lead through the process of creating, distributing and certifying photonic entanglement in various degrees of freedom with a range of different methods. The wavelength in all publications lies in the C-band of modern telecommunication and thus the research conducted within this thesis represents a stepping stone towards future quantum information networks.

BIBLIOGRAPHY

[1] P. G. Kwiat, K. Mattle, H. Weinfurter, A. Zeilinger, A. V. Sergienko, and Y. Shih, "New high-intensity source of polarization-entangled photon pairs," *Phys. Rev. Lett.*, vol. 75, pp. 4337–4341, Dec 1995.

[2] J. A. Formaggio, D. I. Kaiser, M. M. Murskyj, and T. E. Weiss, "Violation of the leggett-garg inequality in neutrino oscillations," *Phys. Rev. Lett.*, vol. 117, p. 050402, Jul 2016.

[3] B. Hensen, H. Bernien, A. E. Dréau, A. Reiserer, N. Kalb, M. S. Blok, J. Ruitenberg, R. F. L. Vermeulen, R. N. Schouten, C. Abellán, W. Amaya, V. Pruneri, M. W. Mitchell, M. Markham, D. J. Twitchen, D. Elkouss, S. Wehner, T. H. Taminiau, and R. Hanson, "Loophole-free bell inequality violation using electron spins separated by 1.3 kilometres," *Nature*, vol. 526, pp. 682–686, Oct 2015.

[4] W. K. Wootters and W. H. Zurek, "A single quantum cannot be cloned," *Nature*, vol. 299, no. 5886, pp. 802–803, 1982.

[5] R. Ursin, F. Tiefenbacher, T. Schmitt-Manderbach, H. Weier, T. Scheidl, M. Lindenthal, B. Blauensteiner, T. Jennewein, J. Perdigues, P. Trojek, B. Ömer, M. Fürst, M. Meyenburg, J. Rarity, Z. Sodnik, C. Barbieri, H. Weinfurter, and A. Zeilinger, "Entanglement-based quantum communication over 144 km," *Nature Physics*, vol. 3, pp. 481–486, June 2007.

[6] S. Wengerowsky, S. K. Joshi, F. Steinlechner, H. Hübel, and R. Ursin, "An entanglement-based wavelength-multiplexed quantum communication network," *Nature*, vol. 564, pp. 225–228, Dec 2018.

[7] T. Jennewein, C. Simon, G. Weihs, H. Weinfurter, and A. Zeilinger, "Quantum cryptography with entangled photons," *Phys. Rev. Lett.*, vol. 84, pp. 4729–4732, May 2000.

[8] K. Mattle, H. Weinfurter, P. G. Kwiat, and A. Zeilinger, "Dense coding in experimental quantum communication," *Phys. Rev. Lett.*, vol. 76, pp. 4656–4659, Jun 1996.

[9] J. T. Barreiro, T.-C. Wei, and P. G. Kwiat, "Beating the channel capacity limit for linear photonic superdense coding," *Nature Physics*, vol. 4, pp. 282–286, Apr 2008.

[10] X.-M. Hu, Y. Guo, B.-H. Liu, Y.-F. Huang, C.-F. Li, and G.-C. Guo, "Beating the channel capacity limit for superdense coding with entangled ququarts," *Science Advances*, vol. 4, no. 7, p. eaat9304, 2018.

[11] F. Arute, K. Arya, and R. Babbush et. al., "Quantum supremacy using a programmable superconducting processor," *Nature*, vol. 574, no. 5, pp. 505–510, 2019.

[12] A. Steane, "Quantum computing," *Reports on Progress in Physics*, vol. 61, pp. 117–173, feb 1998.

[13] S. Barz, E. Kashefi, A. Broadbent, J. F. Fitzsimons, A. Zeilinger, and P. Walther, "Demonstration of blind quantum computing," *Science*, vol. 335, no. 6066, pp. 303–308, 2012.

[14] D. Bouwmeester, J.-W. Pan, K. Mattle, M. Eibl, H. Weinfurter, and A. Zeilinger, "Experimental quantum teleportation," *Nature*, vol. 390, no. 6660, pp. 575–579, 1997.

[15] T. M. Graham, H. J. Bernstein, T.-C. Wei, M. Junge, and P. G. Kwiat, "Superdense teleportation using hyperentangled photons," *Nature Communications*, vol. 6, p. 7185, May 2015.

[16] A. Einstein, B. Podolsky, and N. Rosen, "Can quantum-mechanical description of physical reality be considered complete?," *Phys. Rev.*, vol. 47, pp. 777–780, May 1935.

[17] W. Heisenberg, "Über den anschaulichen inhalt der quantentheoretischen kinematik und mechanik," *Zeitschrift für Physik*, vol. 43, no. 3, pp. 172–198, 1927.

[18] G. C. Ghirardi, A. Rimini, and T. Weber, "A general argument against superluminal transmission through the quantum mechanical measurement process," *Lettere al Nuovo Cimento*, vol. 27, pp. 293–298, Mar 1980.

[19] P. A. M. Dirac, "A new notation for quantum mechanics," *Mathematical Proceedings of the Cambridge Philosophical Society*, vol. 35, no. 3, p. 416–418, 1939.

[20] P. G. Kwiat, A. M. Steinberg, and R. Y. Chiao, "High-visibility interference in a bell-inequality experiment for energy and time," *Phys. Rev. A*, vol. 47, pp. R2472–R2475, Apr 1993.

[21] J. C. Howell, R. S. Bennink, S. J. Bentley, and R. W. Boyd, "Realization of the einstein-podolsky-rosen paradox using momentum- and position-entangled photons from spontaneous parametric down conversion," *Phys. Rev. Lett.*, vol. 92, p. 210403, May 2004.

[22] A. Mair, A. Vaziri, G. Weihs, and A. Zeilinger, "Entanglement of the orbital angular momentum states of photons," *Nature*, vol. 412, pp. 313–316, Oct 2015.

[23] M. Avenhaus, M. V. Chekhova, L. A. Krivitsky, G. Leuchs, and C. Silberhorn, "Experimental verification of high spectral entanglement for pulsed waveguided spontaneous parametric down-conversion," *Phys. Rev. A*, vol. 79, p. 043836, Apr 2009.

[24] S. C. Wein, J. C. Loredo, M. Maffei, P. Hilaire, A. Harouri, N. Somaschi, A. Lemaître, I. Sagnes, L. Lanco, O. Krebs, A. Auffèves, C. Simon, P. Senellart, and C. Antón-Solanas, "Photon-number entanglement generated by sequential excitation of a two-level atom," *Nature Photonics*, vol. 16, pp. 374–379, May 2022.

[25] F.-G. Deng, B.-C. Ren, and X.-H. Li, "Quantum hyperentanglement and its applications in quantum information processing," *Science Bulletin*, vol. 62, no. 1, pp. 46–68, 2017.

[26] P. G. Kwiat, "Hyper-entangled states," *Journal of Modern Optics*, vol. 44, no. 11-12, pp. 2173–2184, 1997.

[27] J. T. Barreiro, N. K. Langford, N. A. Peters, and P. G. Kwiat, "Generation of hyperentangled photon pairs," *Phys. Rev. Lett.*, vol. 95, p. 260501, Dec 2005.

[28] J. C. Chapman, C. C. W. Lim, and P. G. Kwiat, "Hyperentangled time-bin and polarization quantum key distribution," 2019.

[29] J. Suo, S. Dong, W. Zhang, Y. Huang, and J. Peng, "Generation of hyperentanglement on polarization and energy-time based on a silicon micro-ring cavity," *Opt. Express*, vol. 23, pp. 3985–3995, Feb 2015.

[30] S. Walborn, C. Monken, S. Pádua, and P. Souto Ribeiro, "Spatial correlations in parametric down-conversion," *Physics Reports*, vol. 495, no. 4, pp. 87 – 139, 2010.

[31] T. Kim, M. Fiorentino, and F. N. C. Wong, "Phase-stable source of polarization-entangled photons using a polarization sagnac interferometer," *Phys. Rev. A*, vol. 73, p. 012316, Jan 2006.

[32] J. D. Franson, "Bell inequality for position and time," *Phys. Rev. Lett.*, vol. 62, pp. 2205–2208, May 1989.

[33] S. Kraft, A. Deninger, C. Trück, J. Fortágh, F. Lison, and C. Zimmermann, "Rubidium spectroscopy at 778–780 nm with a distributed feedback laser diode," *Laser Physics Letters*, vol. 2, p. 71, nov 2004.

[34] J. Yin, J.-G. Ren, H. Lu, Y. Cao, H.-L. Yong, Y.-P. Wu, C. Liu, S.-K. Liao, F. Zhou, Y. Jiang, X.-D. Cai, P. Xu, G.-S. Pan, J.-J. Jia, Y.-M. Huang, H. Yin, J.-Y. Wang, Y.-A. Chen, C.-Z. Peng, and J.-W. Pan, "Quantum teleportation and entanglement distribution over 100-kilometre free-space channels," *Nature*, vol. 488, pp. 185–188, Aug. 2012.

[35] F. Steinlechner, S. Ecker, M. Fink, B. Liu, J. Bavaresco, M. Huber, T. Scheidl, and R. Ursin, "Distribution of high-dimensional entanglement via an intra-city free-space link," *Nature Communications*, vol. 8, p. 15971, Jul 2017.

[36] J. Yin, Y. Cao, Y.-H. Li, S.-K. Liao, L. Zhang, J.-G. Ren, W.-Q. Cai, W.-Y. Liu, B. Li, H. Dai, G.-B. Li, Q.-M. Lu, Y.-H. Gong, Y. Xu, S.-L. Li, F.-Z. Li, Y.-Y. Yin, Z.-Q. Jiang, M. Li, J.-J. Jia, G. Ren, D. He, Y.-L. Zhou, X.-X. Zhang, N. Wang, X. Chang, Z.-C. Zhu, N.-L. Liu, Y.-A. Chen, C.-Y. Lu, R. Shu, C.-Z. Peng, J.-Y. Wang, and J.-W. Pan, "Satellite-based entanglement distribution over 1200 kilometers," *Science*, vol. 356, no. 6343, pp. 1140–1144, 2017.

[37] S.-K. Liao, W.-Q. Cai, J. Handsteiner, B. Liu, J. Yin, L. Zhang, D. Rauch, M. Fink, J.-G. Ren, W.-Y. Liu, Y. Li, Q. Shen, Y. Cao, F.-Z. Li, J.-F. Wang, Y.-M. Huang, L. Deng, T. Xi, L. Ma, T. Hu, L. Li, N.-L. Liu, F. Koidl, P. Wang, Y.-A. Chen, X.-B. Wang, M. Steindorfer, G. Kirchner, C.-Y. Lu, R. Shu, R. Ursin, T. Scheidl, C.-Z. Peng, J.-Y. Wang, A. Zeilinger, and J.-W. Pan, "Satellite-relayed intercontinental quantum network," *Phys. Rev. Lett.*, vol. 120, p. 030501, Jan 2018.

[38] B. Korzh, C. C. W. Lim, R. Houlmann, N. Gisin, M. J. Li, D. Nolan, B. Sanguinetti, R. Thew, and H. Zbinden, "Provably secure and practical quantum key distribution over 307 km of optical fibre," *Nature Photonics*, vol. 9, pp. 163–168, Feb. 2015.

[39] A. Boaron, G. Boso, D. Rusca, C. Vulliez, C. Autebert, M. Caloz, M. Perrenoud, G. Gras, F. Bussières, M.-J. Li, D. Nolan, A. Martin, and H. Zbinden, "Secure quantum key distribution over 421 km of optical fiber," *Phys. Rev. Lett.*, vol. 121, p. 190502, Nov 2018.

[40] S. Wengerowsky, S. K. Joshi, F. Steinlechner, J. R. Zichi, B. Liu, T. Scheidl, S. M. Dobrovolskiy, R. van der Molen, J. W. N. Los, V. Zwiller, M. A. M. Versteegh, A. Mura, D. Calonico, M. Inguscio, A. Zeilinger, A. Xuereb, and R. Ursin, "Passively stable distribution of polarisation entanglement over 192 km of deployed optical fibre," *npj Quantum Information*, vol. 6, Jan. 2020.

[41] S. Neumann, A. Buchner, L. Bulla, M. Bohmann, and R. Ursin, "Continuous entanglement distribution over a transnational 248 km fibre link," 2022.

[42] G. B. Xavier and G. Lima, "Quantum information processing with space-division multiplexing optical fibres," *Communications Physics*, vol. 3, p. 9, Jan 2020.

[43] K. Saitoh and S. Matsuo, "Multicore fiber technology," *J. Lightwave Technol.*, vol. 34, pp. 55–66, Jan 2016.

[44] B. P. Williams, R. J. Sadlier, and T. S. Humble, "Superdense coding over optical fiber links with complete bell-state measurements," *Phys. Rev. Lett.*, vol. 118, p. 050501, Feb 2017.

[45] S. Ecker, F. Bouchard, L. Bulla, F. Brandt, O. Kohout, F. Steinlechner, R. Fickler, M. Malik, Y. Guryanova, R. Ursin, and M. Huber, "Overcoming noise in entanglement distribution," *Phys. Rev. X*, vol. 9, p. 041042, Nov 2019.

[46] M. Doda, M. Huber, G. Murta, M. Pivoluska, M. Plesch, and C. Vlachou, "Quantum key distribution overcoming extreme noise: Simultaneous subspace coding using high-dimensional entanglement," *Phys. Rev. Applied*, vol. 15, p. 034003, Mar 2021.

[47] X.-M. Hu, C. Zhang, Y. Guo, F.-X. Wang, W.-B. Xing, C.-X. Huang, B.-H. Liu, Y.-F. Huang, C.-F. Li, G.-C. Guo, X. Gao, M. Pivoluska, and M. Huber, "Pathways for entanglement based quantum communication in the face of high noise," 2020.

[48] E. A. Ortega, K. Dovzhik, J. Fuenzalida, S. Wengerowsky, J. C. Alvarado-Zacarias, R. F. Shiozaki, R. Amezcua-Correa, M. Bohmann, and R. Ursin, "Experimental space-division multiplexed polarization-entanglement distribution through 12 paths of a multicore fiber," *PRX Quantum*, vol. 2, p. 040356, Dec 2021.

[49] J. S. Bell, "On the einstein podolsky rosen paradox," *Physics Physique Fizika*, vol. 1, pp. 195–200, Nov 1964.

[50] M. A. Nielsen and I. L. Chuang, *Quantum Computation and Quantum Information: 10th Anniversary Edition*. Cambridge University Press, 2010.

[51] C. K. Law and J. H. Eberly, "Analysis and interpretation of high transverse entanglement in optical parametric down conversion," *Phys. Rev. Lett.*, vol. 92, p. 127903, Mar 2004.

[52] M. J. Bastiaans, "The wigner distribution function of partially coherent light," *Optica Acta: International Journal of Optics*, vol. 28, no. 9, pp. 1215–1224, 1981.

[53] H. D. L. Pires, C. H. Monken, and M. P. van Exter, "Direct measurement of transverse-mode entanglement in two-photon states," *Phys. Rev. A*, vol. 80, no. 2, p. 022307, 2009.

[54] J. F. Clauser, M. A. Horne, A. Shimony, and R. A. Holt, "Proposed experiment to test local hidden-variable theories," *Phys. Rev. Lett.*, vol. 23, pp. 880–884, Oct 1969.

[55] M. D. Reid, "Demonstration of the einstein-podolsky-rosen paradox using nondegenerate parametric amplification," *Phys. Rev. A*, vol. 40, pp. 913–923, Jul 1989.

[56] E. G. Cavalcanti, S. J. Jones, H. M. Wiseman, and M. D. Reid, "Experimental criteria for steering and the einstein-podolsky-rosen paradox," *Phys. Rev. A*, vol. 80, p. 032112, Sep 2009.

[57] M. D. Reid, P. D. Drummond, W. P. Bowen, E. G. Cavalcanti, P. K. Lam, H. A. Bachor, U. L. Andersen, and G. Leuchs, "Colloquium: The einstein-podolsky-rosen paradox: From concepts to applications," *Rev. Mod. Phys.*, vol. 81, pp. 1727–1751, Dec 2009.

[58] H. Bechmann-Pasquinucci and W. Tittel, "Quantum cryptography using larger alphabets," *Phys. Rev. A*, vol. 61, p. 062308, May 2000.

[59] I. Ali-Khan, C. J. Broadbent, and J. C. Howell, "Large-alphabet quantum key distribution using energy-time entangled bipartite states," *Phys. Rev. Lett.*, vol. 98, p. 060503, Feb 2007.

[60] A. Martin, T. Guerreiro, A. Tiranov, S. Designolle, F. Fröwis, N. Brunner, M. Huber, and N. Gisin, "Quantifying photonic high-dimensional entanglement," *Phys. Rev. Lett.*, vol. 118, p. 110501, Mar 2017.

[61] P.-I. Dietrich, R. J. Harris, M. Blaicher, M. K. Corrigan, T. J. Morris, W. Freude, A. Quirrenbach, and C. Koos, "Printed freeform lens arrays on multi-core fibers for highly efficient coupling in astrophotonic systems," *Opt. Express*, vol. 25, pp. 18288–18295, Jul 2017.

[62] A. K. Ghatak and K. Thyagarajan, "Optical waveguides and fibers," *Fundamentals of Photonics*, vol. Chapter 7, 2008.

[63] M. P. Almeida, S. P. Walborn, and P. H. Souto Ribeiro, "Experimental investigation of quantum key distribution with position and momentum of photon pairs," *Phys. Rev. A*, vol. 72, p. 022313, Aug 2005.

[64] D. S. Tasca, R. M. Gomes, F. Toscano, P. H. Souto Ribeiro, and S. P. Walborn, "Continuous-variable quantum computation with spatial degrees of freedom of photons," *Phys. Rev. A*, vol. 83, p. 052325, May 2011.

[65] T. B. Pittman, Y. H. Shih, D. V. Strekalov, and A. V. Sergienko, "Optical imaging by means of two-photon quantum entanglement," *Phys. Rev. A*, vol. 52, pp. R3429–R3432, Nov 1995.

[66] C. H. Bennett and S. J. Wiesner, "Communication via one- and two-particle operators on einstein-podolsky-rosen states," *Phys. Rev. Lett.*, vol. 69, pp. 2881–2884, Nov 1992.